Department of Precision and Microsystems Engineering

# Employing Sensitivity Analysis for Evaluation of Vibration Effects on Multi-Mirror Optomechanical Systems

A.T.F. Postma

Report no : 2024.017
Professor : Nandini Bhattacharya
Specialisation : Optomechatronics
Type of report : Master Thesis
Date : March 27, 2024

# Employing Sensitivity Analysis for Evaluation of Vibration Effects on Multi-Mirror Optomechanical Systems

by

A.T.F. Postma

| | | |
|---|---|---|
| Student number: | 4553589 | |
| Thesis committee: | Dr. Ir. N. Bhattacharya | TU Delft, supervisor |
| | Ir. F.C.M. van Kempen | TNO, supervisor |
| | Dr. Ir. S.J. van den Boom | TNO, supervisor |
| | Dr. Ir. S.M.B. Bäumer | TNO, committee member |
| | Dr. Ir. J.F.L. Goosen | TU Delft, committee member |
| | Dr. Ir. F. Bociort | TU Delft, committee member |
| Project Duration: | March, 2023 - March, 2024 | |
| Faculty: | Faculty of Mechanical Engineering, Delft | |

TU Delft

# Abstract

This study presents a novel approach for evaluating the effects of dynamic disturbances on optical performance using sensitivity analysis. The computation of optical performance for perturbed optical systems is too costly with state-of-the-art analysis software when applied in the use case for the optimization of the optomechanical interface, and therefore using a simplified model, based on ray transfer matrices, describing the most critical phenomena provides a solution. The proposed analytical framework employs a Taylor expansion for the merit function, incorporating both the Jacobian and Hessian matrices, to reduce computation time in transient analysis. The effect of small perturbations on the merit function is found to be accurately described by the approximation when solely the Jacobian is included, for larger displacement fields the approximation deviates significantly without the inclusion of the Hessian. Next to this, the definition of a grating matrix is appended to the framework to facilitate the analysis of a larger set of systems. For transient analysis, the proposed framework exhibits a remarkable improvement in computation time, with minimal degradation in accuracy for paraxial systems. All findings hold relevance for the effect of rigid body displacements in coupled mechanical-optical analyses and further optimization of this coupling under disturbed conditions.

# Preface

With the submission of this thesis, my days as a student come to an end. During this period I learned an invaluable amount of hard and soft skills, and I was able to do this with a group of amazing people around me. The environment in the university to constantly grow and learn is something I have always cherished and will become a prerequisite for my, yet unknown, endeavor. As for the last year, I want to thank TNO for the possibility of collaborating on this thesis with special thanks to Floris van Kempen and Sanne van den Boom. Their guidance throughout this project made me critical of my work and helped me formulate my thoughts clearly on paper. During this year the hard days can be counted on only one hand, and their time to discuss the research when I felt stuck has played a significant role in that. From the TU Delft, I want to thank Nandini Bhattacharya for setting my learning curve within this research as the main priority, I have always felt supported in researching possible research directions. Signing my diploma may seem like an individual performance, however, without the help from my friends, Daphne and my parents, it may have taken a few more months and I am very thankful for them.

*A.T.F. Postma*
*Delft, March 2024*

# Contents

# 1

# Introduction

Nowadays, optical instrumentation is increasingly optimized for optical performance in order to achieve high measurement precision, often while being constrained to a small volume and strict mass requirements. Typically, this optomechanical design optimization leads to instruments that are sensitive to perturbations from the nominal design. For instance, vibrations may cause inaccurate measurement readings in optical systems, which could lead to false conclusions on the acquired data. These effects of vibrations can be countered actively or passively, with both requiring an understanding of the disturbance itself and the impact on the instrument's performance. Rapid assessment of the impact of vibrations on the optical performance provides valuable insights for the engineers designing the instrument, and is an important step towards opto-mechanical design optimization. This optimization enables the discovery of the optimum configuration for an optomechanical interface and facilitates measures to passively counteract preconceived disturbance effects. In this thesis, the change in optical performance is analytically evaluated for rigid body displacements of optical elements within a system, where the analytical analysis facilitates the rapid and cost-effective computation of gradients with applications in time-dependent optomechanical analysis in gradient-based optimization.

Many studies have been performed on the effect of thermal disturbances on optical performance, this field is known as Structural Thermal Optical Performance (STOP) analysis[1, 26]. The optical performance, in this field of research, is mostly computed by existing optical analysis software coupled to external (thermo)mechanical analysis software which leads to large computation times e.g. when transient outcomes are studied. This results from recalculating the optical performance with a complete ray tracing analysis at each time instant while neglecting the information on the merit function evaluation from the previous instant. While some effort has been made by Hahn *et al.*[15] to find fast computation of transient solutions for the performance of a disturbed single lens, this model for transient analysis does not apply to the performance analysis of multi-mirror optical systems. The intrinsic cross-dependence of multiple variables across different objects within the system is not captured and could be shown by sensitivity analysis. The field of transient performance calculation has not received significant attention and therefore the accuracy and applicability of the analytical framework, based on ray transfer matrices, is researched for this field of research.

## 1.1. Research questions

The goal of this research is to establish an analytical framework for the performance calculation of optical systems and to extract sensitivities. The analytical framework is promised to be a powerful technique for optical performance analysis since sensitivity analysis should decrease computation time when related to transient analysis in Zemax or optimization iterations for optomechanical interfaces. This resulted in the following research question with relative sub-questions:

*Main research question: How can sensitivity analysis be utilized to evaluate and understand the effects of dynamic disturbances on the optical performance of a multi-mirror optomechanical system?*

- What characteristics must the analytical framework possess to accommodate rigid body displacements, and which optical elements can be integrated within the framework?
- What is the accuracy of the computational results and sensitivities obtained through the analytical framework for a multi-mirror optical system?
- How does the approximation of the merit function improve when mixed-partial derivatives are taken into account?
- How does the approximation on the merit function perform on transient analysis when compared to existing state-of-the-art analysis software, taking into account accuracy, computation time, and the order of derivatives?

## 1.2. Project lay out

The thesis is segmented into three parts: Literature Review and Model selection, Model Verification and Sensitivities, and Application. In the Literature Review and Model selection, multiple matrix formulations for ray optics are discussed and the consequences of rigid body displacements are related to different merit functions for optical systems. The body of Verification and Sensitivities starts with chapter 5 and explains the chosen merit functions and how the matrix formulation applies to it. In chapter 6, the analytical framework is verified on its performance and accuracy for the sensitivities with analysis in Zemax. This part finishes with introducing the new matrix formulation for a grating and can be read in chapter 7. The part Application includes chapter 8 and chapter 9, which discusses the application of the analytical framework to a Czerny-Turner spectrometer, and the expansion toward transient analysis with displacement fields from Comsol. Lastly, in chapter 10 the conclusions are stated with accompanying recommendations.

# 2

# Literature Review

## 2.1. Geometrical Optics

Before evaluating the performance of an optical instrument, an understanding of light propagation needs to be established. This chapter introduces the reader to the propagation model of geometrical optics and its connection to wave optics. At the end of the chapter, the different formulations of rays and matrices are discussed.

### Ray optics

The concept of geometrical optics stems back to the Greek era. The work of Euclid, a mathematician, is estimated to be written around 300 BC and delves into the explanation of vision [33]. It describes how different rays entering the eye are perceived. The definition for the ray “is an oriented curve which is everywhere perpendicular to the surface of constant phase and points in the direction of the flow of energy” [32]. This propagation is schematically shown in Figure 2.1.

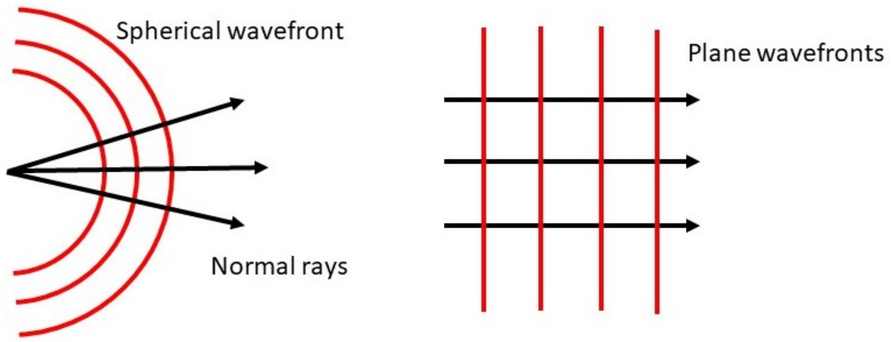

**Figure 2.1:** Schematic representation of the relation between wave and ray propagation. The black arrows depict rays and show how rays propagate in relation to the propagation of spherical and plane wavefronts

Spherical wavefronts are observed in radiating light of point sources and are assumed to become planar wavefronts over large distances. The common property for the different wavefronts is that rays propagate perpendicular to the wavefront.

**Refraction and reflection** Redirecting light can be performed via two different methods, namely refraction and reflection. Both techniques are justified by the principle of Fermat, and equations are derived from this. The principle states that “The path followed by a light ray between two points is the one that takes the least amount of time” (Fermat, 1657). For reflection, the derivation shows that the angle of the incoming light ray is equal to the angle of the outgoing ray with respect to the normal of the reflecting surface. On the other hand, the result of the derivation for refraction is given in Snell's law. The formula for reflection is given by

$$\theta_i = \theta_r \tag{2.1}$$

and Snell's law is given by

$$n_i \cdot \sin(\theta_i) = n_r \cdot \sin(\theta_r). \tag{2.2}$$

The subscript $i$ stands for incoming ray, and $r$ for reflected ray. The refractive index of the medium in which the ray travels is denoted by $n$. The variable $\theta$ represents the angle the ray makes with the normal of the surface.

**Assumptions** Within geometrical optics, the primary assumption used is known as the paraxial approximation. This approximation makes use of only the first order in the Taylor expansion for the angle ($\theta$) variable. It assumes that angles are small which simplifies the trigonometric relations of rays propagating through the system. The consequence of this is that ray tracing loses its accuracy when rays have an angle larger than approximately 30 degrees with the optical axis. Another result of this assumption is that diffraction can not be described by this method.

Next to this, it is stated by Kidger and Urbach that geometrical optics is only valid when the wavelength approaches zero relative to the system's sizing [19, 32]. Geometrical optics becomes inaccurate for analysis when the traced rays fail to maintain this requirement or exceed the boundaries set by the paraxial approximation. For this reason, the systems that will be regarded during this study should always be dimensioned properly to adhere to both requirements.

### Wave optics

The nature of light can also be described by waves. The work of Maxwell presented that light is a form of electromagnetic radiation, and propagates in waves [27]. With this wave theory, the following phenomena of Interference and Diffraction, Wavefront aberration, and Polarization can be explained.

The comprising theory of light as a wave provides greater precision but the downside is that it is more complex than geometrical optics. To form insights into a perturbed optical system, the wave theory overcomplicates the computation. This will lead to longer computations and a need for an understanding of mathematical subjects such as differential equations.

## Matrix formulations in geometrical optics

Ray tracing can be performed for 2D and 3D systems. Due to the paraxial approximation, the propagation in both dimensions can be computed by linear relations, which are directly described using matrices. This section will first introduce how ray tracing is executed for 2D systems and how these systems are defined, and later the connection to 3D systems will be shown.

**ABCD matrix** Rays as explained in section 2.1 can be described by height and an angle in 2D, where both quantities are both with respect to the optical axis. This formulation is presented by Fowles [13] and is constructed as

$$\begin{pmatrix} h' \\ \theta' \end{pmatrix} = \begin{pmatrix} A & B \\ C & D \end{pmatrix} \begin{pmatrix} h \\ \theta \end{pmatrix} \tag{2.3}$$

In this formulation, $h$ represents the height, and $\theta$ stands for the angle of the ray with the optical axis. The prime on the variable distinguishes the new quantities of the ray after the ABCD operator. Figure 2.2 shows how the quantities relate to the optical axis.

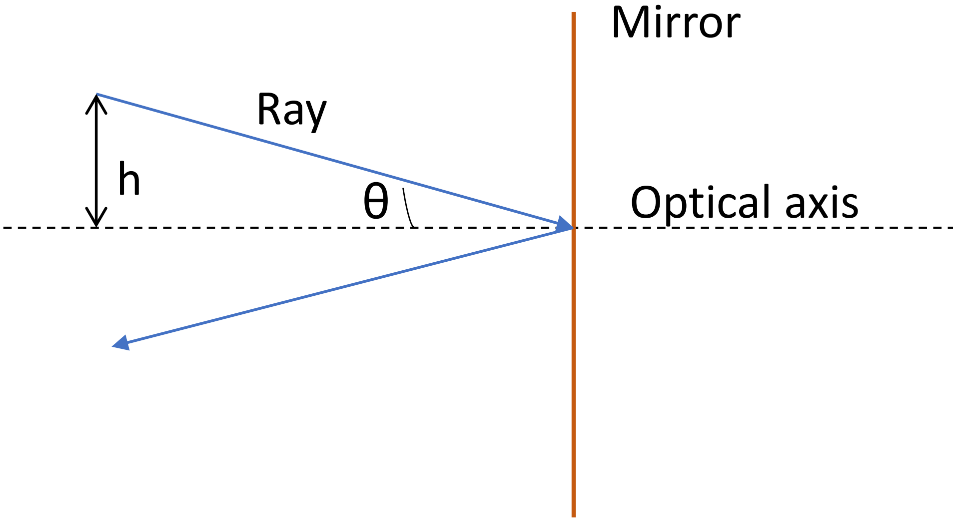

**Figure 2.2:** Schematic overview of reflected ray on a mirror, with the quantities $h$ and $\theta$ depicted with respect to the optical axis

Examples of operators are propagation, reflection, and refraction. All operations can be presented by an ABCD matrix and use the paraxial approximation. Multiplication of the ray with the respective operator matrix computes the new direction and height of the ray. In table 2.1 the matrices for the different operations are shown.

| | |
|---|---|
| $\begin{pmatrix} 1 & d \\ 0 & 1 \end{pmatrix}$ | **Freespace**<br>The symbol $d$ represents travel distance from initial point to next surface |
| $\begin{pmatrix} 1 & 0 \\ 0 & 1 \end{pmatrix}$ | **Flat mirror reflection**<br>The mirror is situated perpendicular to the optical axis, therefore the angle of reflection is incorporated inside the ray vector. As seen in figure 2.2. |
| $\begin{pmatrix} 1 & 0 \\ -\frac{2}{R \cdot cos(\theta)} & 1 \end{pmatrix}$ | **Spherical mirror reflection**<br>The variable $\theta$ represents the angle the mirror makes with the tangential plane, $R$ denotes the radius of curvature. |

**Table 2.1:** ABCD matrices for different operators

**Definition change for 2D** In addition to the ABCD method, an alternative approach to formulating rays has been presented by Corcovilos in 2022 [7]. Corcovilos' method describes rays as linear lines in Cartesian coordinates, with the coefficients of the line serving as the basis for the formulation. To facilitate this change the 2x2 ABCD matrix is transformed into a 3x3 matrix. The extra storage inside these matrices is used to create an operator that can store information about the spatial changes of the elements. The significance of this supplementary information is discussed in section 2.3.

The paraxial approximation is still of effect for this method, therefore the accuracy is not significantly improved in this regard. Nevertheless, the formulation has an advantage in the description of tilted mirrors. The angle the ray makes with the mirror remains unaffected by the paraxial approximation, leading to a more accurate representation of mirrors tilted further than approximately 30 degrees.

Dupraz *et al.*[11] reported an additional description of the ABCD matrix. The proposed matrices are generalized so that it is applicable to any surface in two dimensions. The description of the surface is differentiated, with the effect that each incoming ray is able to reflect with a different curvature and associated normal.

**Connection to 3D** Breakthrough in precise production techniques of mirrors led to the introduction of using freeform mirrors in optical instruments. Freeform mirrors show great improvements in the correction of aberrations and can even minimize the number of elements needed to obtain the required performance [31]. Next to different curvatures in the x and y-axes, an extra polynomial function can be given to the optical surface that describes the sag. Due to this extra polynomial function, optical systems lose their rotationally symmetric feature, and 2D ray tracers can not be applied. For this reason, new methods are developed to trace rays in optical systems that make use of freeform surfaces.

The application of the ABCD method for ray tracing can be extended to 3D optical systems when the expression of the surface is only given by different curvatures. This involves the addition of another ABCD matrix along the diagonal, effectively creating a 4x4 matrix. Although both Corcovilos [7] and Dupraz *et al.*[11] mention that their method offers 3D capabilities, nothing has been practically applied as of now.

The group of Dain Lin has an extensive publication record in the field of ray tracing. In 2006 they published a ray trace method that includes the first-order [24], and later in 2020 they extended this method to third-order [21] both for flat and spherical surfaces. Both methods focus on skew rays in an optical system, and explain that the fifth-order of the Taylor expansion of the $\theta$-angle can be more accurately described by finite differencing while including the third-order. The method described for first-order is clearly written and its matrices are shared, for third-order, this information is missing and the publications focus more on the deduction of how to include higher orders.

Ray tracing within systems featuring freeform surfaces is presented by Caron *et al.*[5]. The method proposes to use higher orders of the ray variables in the Taylor expansion. Therefore the matrix operators grow in size to 34x34 and aberrations that are affected by higher order errors can be described by this method. The freeform surface description that is deployed in the theory is based on a polynomial expansion with curvature coefficients for the x and y-axes, and five coefficients that represent the plane-symmetric freeform surfaces.

The different theories on the propagation of light are addressed in this chapter. This showed that the linearization of the propagation of light within geometrical optics helps in creating a simple analytical model. This method has become standard in the industry, and different variations exist for systems in 2D and 3D. chapter 3 delves into a more thorough comparison between all the above-mentioned formulations and concludes on what method to use for the analytical framework.

## 2.2. Optical analysis

In optical instruments, light is utilized to obtain images or measure objects and phenomena that can be invisible to the naked eye. Prior to the application of instruments, an analysis of their performance is essential to ensure meeting the requirements of the system. This chapter will go into depth about how the analysis is performed and the different requirements optical systems can be held to. During operation, the performance may change due to environmental perturbations, resulting in a need for an error budget. The structure of the error budget will be discussed and lastly, this chapter will discuss the different perturbations that can be encountered.

## Methods for Optical Analysis

A thorough evaluation of the optical design is essential for quantifying its performance. This section will concentrate on the specific techniques employed to evaluate the requirements of the optical design. The evaluation techniques for simple and complicated systems vary and will be discussed in sequence.

For simple optical designs consisting of previously used elements or elements put in a well-known sequence, the analysis consists of matrices as discussed in chapter section 2.1. The design method of these systems is mainly based on the experience of the designer and empirical data, so basic computations are valid for the quantification of the performance.

The systems that make use of more advanced mirror and lens surfaces are analyzed with a different technique. The first layout of such a system is done by analytical expressions and matrices, therefore needs more accuracy when reviewing its performance. More accuracy is found in computer programs that are able to review both wave and ray optics, such programs are Zemax and CodeV. The usage of computer programs is mainly driven by the accuracy and ease of obtaining spot diagrams and finding the wavefront aberration in the image plane.

In the situation that the optical system underperforms toward the requirements, optimization can be applied. Both Zemax and CodeV can include variables in the system to be optimized so that the requirement is met. Understanding the results of the optimization is key since the design space can become large and the designer needs to know if the result is a global or local minimum. For the optimization of wavefront aberration, Bociort devised a method to examine whether the individual Zernike coefficients of the wavefront in the image plane are balanced [2]. Enlarging the design space by including more variables resolves into better designs. However, determining whether the result is optimal remains challenging.

The last method for quantifying the performance of the newly designed optical instrument is done by testing. This technique is of all methods the most expensive and is only operated when the above-mentioned methods are showing promising results. Interferometry can be used for individual element testing and reference shapes are used for freeform surfaces [17]. Reference flats can show the result of one or multiple surfaces in a chosen image plane, outside of the instrument. To validate a part of the system, the results of that test are checked for good agreement with those obtained from Zemax.

## Requirements

The optical requirement for a system depends on the specific application for which the instrument is built. In the first chapter of Fisher *et al.*[12], a large list of possible requirements is mentioned. The most important requirements will be discussed in this section, and why these requirements are applicable to optical systems using mirrors. Unfortunately, the summation of Fisher *et al.*[12] lacks in mentioning an important part of the optical analysis which is the change of polarization state along the optical axis. The polarization state may change, and its accompanying transmission, over longer distances of propagation and interaction with optical elements.

To streamline the considerations for the requirements, this research will not elaborate on the polarization state. To describe this measure, the light should be considered as a wave or the optical path difference should be considered to construct a phase diagram. The emphasis of this section will be on the different optical requirements considered within TNO.

In systems built for laser communication, the field of view (FoV) is important. The image retrieved in the outer corners of the FoV should be imaged as sharp as around the optical axis. In other words, the FoV should be stable across the whole field. Next to this, other important optical measures are stray light and speckles. These two should be taken into consideration since both induce a low signal-to-noise ratio [16]. In general, optical systems are more efficient when a high signal-to-noise ratio is present. The intensity of the light is larger, and therefore the image is better.

A well-known measure within optics is the spot diagram. It shows where the incoming light rays coming from one point in the object plane cross the image plane. When perfect imaging exists, the spot diagram is just a spot. This result is only obtained within geometrical optics and is not achievable when the system is considered with wave optics. Induced aberrations by the system can be reviewed from the shape of the spot diagram. But mostly, the designer wants the spot size to be minimum. When the spot size increases, the image loses sharpness [12].

The last optical measure, root-mean-square (RMS) wavefront error, describes the deviation in the wavefront entering the image plane, and its expected wavefront. Errors in the wavefront cause unwanted distortion (aberrations) in the image and can be measured by a Shack-Hartmann sensor, when testing the system [28]. The expected wavefront in the image plane can have different forms, for this reason, the measured wavefront is not always compared to the spherical wavefront.

As discussed in chapter 2.1, the paraxial approximation in geometrical optics only considers the first order of the Taylor expansion. Certain requirements on optical systems can accurately be described by taking the first order, and others are also affected by higher orders. Optical path difference and wavefront aberration are examples of measures that are not affected by higher orders. However, the spot diagram of a system is correlated to both first and higher orders.

## Error budget

In the case the system is perturbed and subjected to various errors, the performance should remain satisfactory. For this case, the need for an error budget did arise whilst designing optical systems. The budget is categorized into static and dynamic budgets, the entries within these budgets are discussed in this section. The error budget was explained to the writer by Bob Kruizinga, a colleague within TNO.

Entries within the static budget include manufacturing and assembly. Surface roughness is for example closely related to manufacturing and is considered during the design phase. However, manufacturing techniques are prone to underdeliver the requested standards for surface roughness. Next to this, errors can also be introduced by misalignment of optical elements during assembly, this particularly occurs in mass-produced instruments due to errors introduced the production proces.

Vibrations and heat loads are examples of dynamic entries for the error budget. These perturbations occur during operation and their effects should be taken into account for the optical design. Quantifying the dynamic error enables the optical design to be adjusted for these environmental perturbations. In essence, analyzing to a greater extent the amount of error in the system will lead to a more thoroughly devised system, and where to adjust to.

## Perturbations

The dynamic error budget consists of multiple elements, referred to as perturbations. For optical instruments operational in satellites, vibrations and heat loading are perturbations of interest. Research has been published extensively on the effect of heat loading on optical performance. One of the latest largest projects around this subject is explained by Gracey *et al.* [14], they go into detail about the modeling and results for the James Webb Space Telescope (JWST) while being exposed to on-orbit temperature environments. Modeling the effect of heat loading is of interest to optomechanical designers since elements within the system undergo movement and deformation due to temperature gradients, these effects may be attributed to both the material purity and mechanical design. This field of research is referred to as STOP analysis.

The design cycle of the mechanical design for an instrument perturbed by heat loading is extensive and multiple disciplines have to work on the challenge in series. To map the design cycle, and show the gaps where research can be implemented to streamline the process, the flowchart as seen in figure **??** has been constructed. The flowchart is put together with the help of both optical and optomechanical engineers within TNO to provide a comprehensive overview. In the flowchart, the green blocks indicate where research may add to optimize the design cycle. Later, the structure of the flowchart was compared to the flowchart developed by Lyu and Zhan [26], and showed great resemblance.

The impact of vibrations on optical instruments onboard satellites is relatively small since the amplitude of vibrations in space is low. Nevertheless, vibrations become more significant when optical instruments are tested or employed in the airplane's environment. Again, the mechanical design has a great effect on the degradation of optical performance due to this perturbation. By examining the eigenfrequency and its eigenmodes of the housing, insights can be gained into how the perturbation changes the placement of optical elements within the system. The consequences of displacements due to perturbations are further discussed in chapter 2.3.

To summarize, the performance of optical systems can be measured in multiple ways and each measure has its own evaluation method. When choosing a performance measure, the method to evaluate this needs to be thought of carefully. During operation, changes in optical performance arise due to perturbations and are taken into account by creating an error budget. To enhance designs further, a more detailed quantification of the effects of these perturbations is essential.

## 2.3. Consequences of perturbations

This chapter addresses the effects induced by thermal loading and vibrations, namely rigid body displacements and surface deformations. The effects are interlinked as they can be mutually represented by each other. After perturbation, the designer needs to split the changes into these factors. First, the rigid body displacements will be discussed in detail, followed by an explanation of their impact on optical performance. In the second part of the chapter, the focus shifts to surface deformations.

### Rigid body displacement

Every element in 3D space knows six different motions and can be seen in figure 2.3. XD, YD, and ZD are the translation on the x,y, and z axis respectively where the z-axis is the optical axis. XR, YR, and ZR are the rotations around these axes. In the situation that optical elements are displaced by perturbations, the displacement can be described by these six motions.

One exception to the rule exists for rotationally symmetric systems. In this type of system, the z-axis is the centroid over which the system can rotate 360 degrees. Hence, the spatial change of the element is described in five motions, in other words, the sensitivity on the optical performance is 0.

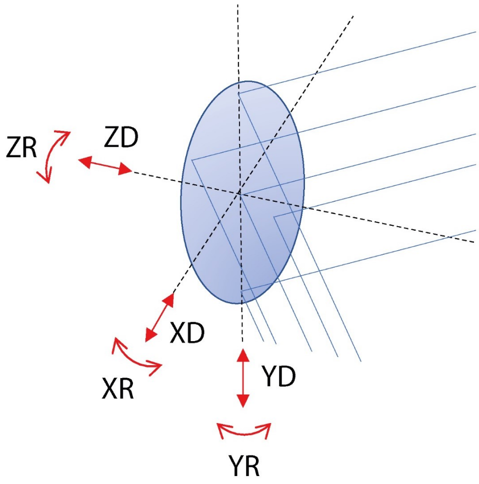

**Figure 2.3:** Six degrees of freedom for a mirror schematically shown

Rigid body motion of mirrors can occur due to thermal expansion induced by heat or vibrating of the housing at its eigenfrequency. In the situation where thermal expansion occurs, nonhomogeneous expansion can implicate rotation or displacement from the housing to the mirror. Next to this, relative distances and rotations might also change when the geometry of the housing allows for that. For vibrations, eigenmodes of the mechanical housing introduce the bending of the complete structure in a sinusoidal manner, resulting in displacements that subsequently lead to optical errors.

**Impact** The influence of a perturbed mirror on the reflected ray correlates with the normal vector. The trajectory of the reflected ray is determined by both the incoming ray's direction and the normal vector. Deviations from the intended normal vector can result in divergent paths, and in larger systems, these discrepancies may accumulate.

The consequences of one perturbed mirror are described clearly by Hvisc [18]. Hvisc argues that "instead of having two elements with very tight tolerances individually, it was found that you could have very tight tolerances for one element relative to the system". This shows that rigid body displacements of elements can be corrected or mitigated by displacements of other elements. The dependencies of these variables are of interest for the creation of a better design.

## Surface deformations

The second effect of perturbations on the optical system is surface deformation. Most of the time, the precise shapes of mirror surfaces are established through optimization. When perturbations change the shape of the surface, the optical performance alters from its optimum.

Reasons for deformations on the surface are temperature changes, mechanical stresses, vibrations, and manufacturing imperfections [39]. Manufacturing can be categorized into the static error budget as discussed in section 2.2 since it is present before applying perturbations. The other sources of deformation will be investigated more thoroughly within this section.

**Temperature changes** Mirrors are placed in/on a mounting, for practicality in transport, handling, and assembly. The description of a mirror that is used in this study only refers to the reflecting surface. This surface can be established from the same block of material as the mounting during manufacturing, and only polishing is done for the required reflectance.

To increase the reflectance further after polishing, surfaces are coated to achieve a higher percentage of reflectance. This is possible since the reflectance of a material is dependent on wavelength. Unfortunately, after this process, the mirror experiences a loss of material homogeneity. The coated surfaces are susceptible to deformation after heat loads are applied. The effects of different expansions can be seen schematically in figure 2.4. The expansion coefficient changes for the layer of coating, and therefore a flat mirror can undergo bending.

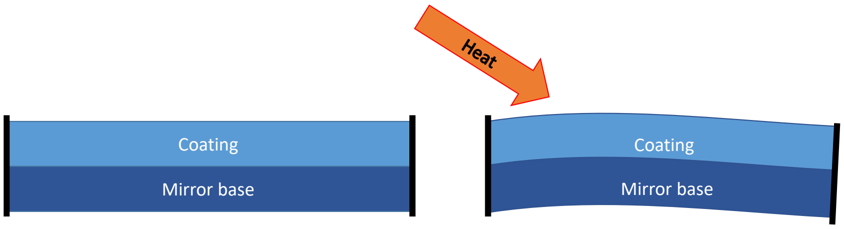

**Figure 2.4:** A schematic overview of the effects of heat loads on a coated mirror

**Mechanical stresses** The mountings for the mirrors are attached to a housing, which holds all optical elements in the correct places. When heat loads are applied, the housing may expand or contract. Since the housing is most of the time from a different material than the mirrors' (due to weight restrictions in space applications), mechanical stresses will occur at the connection points. If mirrors are not assumed to be stiff, this causes the mirror to undergo a bending moment, and therefore a deformation on the surface occurs.

**Vibrations** Surface deformations may also occur due to vibrations when the individual eigenfrequency of the mirror is reached. Mirrors used in optical instruments for satellites are small and low-weight, which leads to relatively high eigenfrequencies. Generally, the eigenfrequency of the housing is lower when contrasted with that of the mirrors, which leads to no surface deformations induced by vibrations.

## 2.4. Sensitivities in optical systems

Sensitivities are used to describe changes in performance when a variable changes and can be helpful for optimization [8]. Mapping the performance changes linked to variables is beneficial for designers. Sensitivities provide numerical proof and insights that support design choices. This means that designers can consider the design of mountings and housings with certain variables in a quantified manner. Insights gained from sensitivities help create designs that are less likely to fail when faced with different boundary conditions given in the optimzer.

This chapter first elaborates on the different methods for obtaining sensitivities and their use cases in the literature. Secondly, sensitivities used for optimization are discussed. Lastly, sensitivities linked to dynamic perturbations will be discussed.

### Different types of sensitivities

Sensitivities can be found via multiple methods, such as analytically, numerically, or through other methods such as using Monte Carlo simulations. Dain Lin *et al.* [8] described the state of sensitivities in optics as non-analytical, since no mathematical function could be differentiated to elaborate on the sensitivities of the optical performance in 2004. This however changed over the last decades and is now more common. The same research group described the optical path length (OPL) and irradiance using an analytical method, namely using the Jacobian and Hessian matrices in 2012 [22]. Here only the elementary optics are analyzed.

Computing sensitivities numerically is slower than analytically because it needs repeated evaluations of an optical model for each perturbation. The advantage of numerical sensitivities is that it is applicable to all systems. Analytical derivation may not be possible when no analytical expressions exist for the function or is non-differentiable. Numerical derivation can be used for these cases and can find approximations for the sensitivities.

Monte Carlo simulations, as typically performed by optical engineers, do not work with derivatives but rather in a probabilistic manner. To perform the sensitivity analysis with this method, a distribution (typically a normal distribution) of perturbations is given as input and it captures the uncertainty and variability of the variables. To draw conclusions with this method, a large set of random samples has to be evaluated to create sensitivities. Because of this, computing the Monte Carlo is computationally inefficient for more complicated systems consisting of many variables since it computes the optical model for each set of variables.

### Methods used in literature to obtain sensitivities

Several authors have described optical systems analytically [5, 3]. However, the formulations described in the papers do not elaborate on finding sensitivities. Next to this, rigid body modes are not included in these models. Blaurock *et al.*[1] briefly discuss the analytical sensitivities calculated for the JWST, where the relation between merit function and temperature is explained and no derivation or surface coefficients are given.

The numerical method for sensitivity analysis is used more in literature. In practice, this method is called Sensitivity Table Method (STM) [30]. With finite differencing the relation of two measured points is compared. The disadvantage of this method is that it can only be used in the linear regime because the method loses accuracy when the optical system is non-linear and higher-order derivatives are neglected. In the research of Sanson, only the first-order derivatives are considered. Hence, the STM can only be valid when the system is paraxial because in this approximation higher-order terms are neglected as well [35].

A Monte Carlo simulation is shown in Blaurock *et al.* [1] for the JWST and discussed in great detail. The wavefront error (WFE) and line of sight (LOS) are expressed under 10% uniform uncertainty. Moreover, within TNO this method is also used. Each variable is placed within a bound in which it can vary. If after the simulation the performance for all possible sets of variables is acceptable, the bounds can also be used as a tolerancing of the optical elements.

### Sensitivities in optimization

Optical systems that are optimized for certain use cases can have the drawback that the thought of design is end-result specific, as emphasized by Bociort [2]. The system only leads to useful designs when the boundary conditions, given to the optimizer, are met. An example of a boundary condition related to the STOP analysis may be the operating temperature. The question that arises is whether the optical performance changes due to this boundary condition and with what magnitude. Sensitivities are a valuable tool to map this and quantify the effect on the optical performance given a certain change of a parameter in a model.

Sensitivities are also widely used in gradient-based optimization algorithms, which can find optimized configurations for a very large number of variables. While this research will not focus on the different gradient-based optimization algorithms and their applications in optimization, it is clear that the efficient computation of sensitivities has great benefits in design optimization.

### Analytical sensitivities for Topology Optimization and Vibrations

As discussed earlier in this chapter, sensitivities are useful inputs for optimization algorithms, for instance for topology optimization which is used to create designs for mountings of mirrors [20]. In this research by Koppen *et al.*, the focus was on reducing the optical errors induced by thermal loads by optimizing the mounting with topology optimization. The optical design consisted of two folded mirrors that accommodated a focussing light beam. Perturbations were introduced by heat and the spot size of the system was analyzed via a ray matrix given by Yuan *et al.*[36]. The findings indicate that it is beneficial to use sensitivities for creating optical designs that perform better when perturbed.

Vibrations introduce jitter and defocus to the image. The effect of vibrations on the optical performance can be predicted with sensitivities. In random vibrations present in for example an aircraft, the value of certain variables does have an uncertainty. How these uncertainties propagate toward the spot size is of interest [34]. A simplification for random vibrations is harmonic vibrations. The displacements of the elements are no longer defined by uncertainty but are described by distributions of displacements. A finite displacement field is necessary to give a finite conclusion about the error created by the displacement field. Analytical sensitivities can create a transfer function from a displacement field toward optical error.

Finite displacement fields, or transient mechanical responses, can be effectively calculated based on eigenfrequency analysis. Finite Element Method (FEM) software packages such as Comsol can be used to do eigenfrequency analyses for mechanical housings and the rigid body displacements and rotations of optical elements can be extracted. Then, due to the orthogonality of the associated eigenmodes, the eigenmode of each eigenfrequency can be superimposed with the help of the forcing function, mode participations and transfer functions for each mode.

These transient mechanical responses may then be used to do an optical analysis for each timestep. But, alternatively, when the sensitivities of optical performance with respect to the mechanical displacements are known, modal superposition extends straightforwardly into the optical domain to calculate the optical performance over time when perturbed by vibrations. This powerful technique will benefit the computation time when compared to a Zemax analysis for each time step. Additonally, this can be used to determine optical responses in the frequency domain.

For both applications, sensitivities will enhance the understanding of the design. Next to this, obtaining these sensitivities analytically helps to improve the calculation speed and applicability to a wide branch of optical systems. A better understanding of design can be used to create better designs or learn from the current designs.

# 3

# Trade-off on Matrix Formulations

This chapter elaborates on the trade-off made between different matrix formulations for evaluating the performance of the optical model. For the evaluation, matrix methods defined for systems in 2D and 3D are discussed. All methods are discussed in section 2.1 and as a continuation of this, this chapter discusses the methods per criteria for the trade-off.

## 3.1. Criteria and weighting

Various criteria were used to rank all methods and during construction of the criteria it was emphasized that they should be independent of each other. Next to this, four criteria are used in the trade-off to avoid small differences between the best and worst-performing methodologies. Moreover, to counter small differences between methods, weights are added to the measures to emphasize the importance of the measures and create distance between the results. In addition, the weights per criterion are non-identical for the same measure of creating distance between results.

The weight for the ease of obtaining rigid body sensitivities is the largest since this is what the method will be used for in the first place. Furthermore, accuracy is important for the description of the model hence the second-highest weight of 0.3. For the scalability criterion, the scalability of the method to other systems is weighted higher due to the introduction of more optical elements such as freeform surfaces. The considered criteria and associated weights can be seen in Table 3.1.

In the trade-off, the scalability of the method is taken into account, to ensure an analytical framework. Methods for systems in 2D are considered to ease calculation and surface descriptions, on the other hand, methods for systems in 3D hold more value for continuation. Therefore, scalability was chosen as the first criterion to relate the different methods to systems in 3D.

Next to the scalability towards 3D, more difficult surface descriptions, such as ellipsoidal and parabolic, can also be introduced to enhance the method. For this reason, the second criterion is introduced to weigh the different methods for the introduction of more complex optical elements in the systems to be analyzed.

The third criterion focuses on the incorporation of rigid body displacements in the method. This is of importance since sensitivities on the displacements are desired as output from the analytical framework.

The chosen method should calculate the performance change due to displacements in the system closely. Since the matrix methods linearize the propagation of light, retrieving higher accuracy for incorporating angles outside of the paraxial approximation is beneficial. This criterion takes into account all simplifications made within the set-up of the matrix formulations.

For the last criterion, the integration of the merit function with the method is considered. The methods have different outputs, and therefore the integration with the merit function is weighed.

The trade-off table with all the weights and scores can be reviewed in Table 3.1. All scores will be explained in the following sections.

**Table 3.1:** Trade-off table

| | 2D | | | 3D | | | |
|---|---|---|---|---|---|---|---|
| | ABCD | Corcovilos | Dupraz | Dain Lin | Caron | Double ABCD | Weighting |
| Scalability to 3D | 5<br>0.75 | 4<br>0.6 | 3<br>0.45 | 6<br>0.9 | 6<br>0.9 | 6<br>0.9 | 0.15 |
| Scalability to other systems | 2<br>0.4 | 3<br>0.6 | 4<br>0.8 | 5<br>1 | 6<br>1.2 | 1<br>0.2 | 0.2 |
| Ease of obtaining rigid body sensitivities | 4<br>1.4 | 6<br>2.1 | 2<br>0.7 | 5<br>1.75 | 1<br>0.35 | 3<br>1.05 | 0.35 |
| Accuracy: all simplifications | 2<br>0.6 | 4<br>1.2 | 3<br>0.9 | 5<br>1.5 | 6<br>1.8 | 1<br>0.3 | 0.3 |
| Sum of indices | 3.15 | 4.5 | 2.85 | 5.15 | 4.25 | 2.45 | 1 |

## 3.2. Scalability to 3D

In this research, ray tracing will be used for performance evaluation of optical systems. However, for the continuation of the analytical framework, the method should be scalable towards 3D or already possess this option. Since the methods that function for systems in 3D already have this option, Dain Lin, Caron, and the Double ABCD all received the same indexing.

The index of ABCD is highest in the section of 3D since the 3D method already exists. The last two methods have mentioned in their paper that there exists no extension to 3D as of now, but both are working on this. Corcovilos is ranked higher since after publishing, Dorst have publicated about the introduction of the method for 3D systems by making some alterations [10].

## 3.3. Scalability to other systems

Next to the scalability of systems in 3D, the proposed ray tracing methods can also be extended to systems that consist of different surface types, lenses, or other optical instruments. Caron includes freeform surfaces for mirrors hence it is ranked the highest for this criterium. Dain Lin also has described prisms and lenses and therefore has index 5.

The ABCD methods score the lowest since there exist only matrices for reflection and refraction of flat and spherical optical surfaces on the same axis. No extension toward different systems is present in this framework.

The last two methods are close to this category. Dupraz had a slight advantage since it differentiates the shape of the optical surface and hence can introduce more complexity when implemented in other systems.

## 3.4. Retrieving sensitivities on rigid body displacements

The setup of each ray trace method differs in the relation and allocation of variables. The dependency of variables in the system is of importance with this criterion and what input and output are used.

The outliers for the criterium are Caron and Corcovilos. The method written by Caron is extensive but does not allow, by its formulations, for rigid body displacements. Since the method is extensive, integration would induce rewriting of the theory.

Corcovilos' method is very well applicable to rigid body displacements since the elements are placed within a global coordinate system and are not dependent on the system's earlier elements or the system's optical axis.

## 3.5. Accuracy: all simplifications

Methods make use of assumptions for the development of tracing rays through the system. Assumptions allow for easy calculations but have the disadvantage of creating inaccuracies in the model. To map the created inaccuracies this criterium is implemented within the trade-off

All methods, except for Caron, include only the first order of the Taylor expansion for the propagation of the traced ray. Therefore Caron is given the highest index for this criterion.

The optical elements in both the methods of Corcovilos and Dain Lin can be placed in a global reference frame, and therefore the mirrors can be put under higher angles than 15 degrees with respect to the optical axis.

Due to the relative placement of the optical axis in the ABCD methods, it is ranked in the lower regime.

## 3.6. Conclusion

The trade-off table shows that in respective categories, Corcovilos' and Dain Lin's formulations are in favor. As a result of this, it was decided to pursue both methods for further research to delve more into the complications that may arise during implementation. In Appendix A, the research conducted for the comparison of both methods can be found.

From this study, it was concluded that the method of Dain Lin showed differences with Snell's law for a simple disturbed model. The rigid body sensitivities were not straightforwardly calculated by the method, however, the method of Corcovilos performed well in this regard. As a result, the method of Corcovilos is executed throughout this research for the analytical framework.

# 4

# Method: Matrix formulation

This chapter focuses more in-depth on the matrix formulation of Corcovilos and its contribution to earlier adopted standard ABCD matrices. Moreover, it explains how these contributions enhance the analysis of the effect of rigid body displacements. First, a general overview is given of the matrix formulation, and second, extra benefits from the method are shown.

The formulation for ray tracing created by Corcovilos is briefly touched upon in section 2.1. This section will discuss in more detail the properties and the operation of the theory. Instead of using the older ray trace formulation as seen in Equation 2.3, the rays traced by Corcovilos' method are formulated by a linear function, namely $-mx + cy - h = 0$. Where the vector of the ray now consists of the coefficients $-h, -m$ and $c$, as represented in

$$\vec{r} = \begin{bmatrix} -h \\ -m \\ c \end{bmatrix}. \tag{4.1}$$

The rays are traced through a global coordinate system where the light source is positioned at the origin by default. In the case that the light source is favored in a different place, the formulation allows the rays entering the optical system to be replaced over the y-axis with the height variable ($r_h$). Moreover, the Numerical Aperture (NA) of the incoming light can be changed by the slope ($r_a$) variable. For the first rays, $c$ is set to 1, such that Equation 4.1 becomes $\vec{r} = [-r_h, -r_a, 1]^T$.

For describing the effects of optical elements, the conventional ABCD matrix is used within the formulation. This results in the following matrix for nonreflecting optical elements

$$M = \begin{bmatrix} A & B & 0 \\ C & D & 0 \\ 0 & 0 & 1 \end{bmatrix}. \tag{4.2}$$

For reflecting elements, the right lower corner entry in the matrix is set to -1 and the left upper matrix also holds different signs in comparison to the regular ABCD matrix. In the formulation by Corcovilos, the matrix for a reflecting flat and spherical mirror are respectively

$$M_{flat} = \begin{bmatrix} -1 & 0 & 0 \\ 0 & 1 & 0 \\ 0 & 0 & -1 \end{bmatrix}, M_{spherical} = \begin{bmatrix} -1 & 0 & 0 \\ 2/R_c & 1 & 0 \\ 0 & 0 & -1 \end{bmatrix}. \tag{4.3}$$

In Equation 4.3, $R_c$ is the radius of curvature for the spherical mirror, where a convex mirror is indicated by a positive value for $R_c$. The extra degree of freedom found inside the new matrix formulation is utilized for the placement and orientation of elements within the global coordinate frame. Moreover, for the orientation, its argument is not linearized within its respective matrix. This facilitates a more precise description of the element in the system. Both matrices are described by

$$R_\theta = \begin{bmatrix} 1 & 0 & 0 \\ 0 & cos\theta & sin\theta \\ 0 & sin\theta & cos\theta \end{bmatrix}, T_{u,v} = \begin{bmatrix} 1 & -u & -v \\ 0 & 1 & 0 \\ 0 & 0 & 1 \end{bmatrix}. \tag{4.4}$$

In these formulations $R_\theta$ is the rotation matrix, where $\theta$ is the angle of the rotation of the optical element counter-clockwise with the z-axis of the global coordinate system. $T_{u,v}$ positions the center of the optical element at the coordinate $(u, v)$.

Rays propagating in the global coordinate system are reflected and/or refracted in the local coordinate frame of each element. For each element, the ray is transformed into the local coordinate frame, reflected or refracted, and transformed back to the global coordinate frame. The above-mentioned matrices function for this and are multiplied as

$$M_i = T_{u_i,v_i} R_{\theta_i} M R_{\theta_i}^{-1} T_{u_i,v_i}^{-1}. \tag{4.5}$$

This multiplication shows that the orientation of each element can be modeled independently within the global coordinate system, due to this, the effect of rigid body displacements can be analyzed thoroughly.

As mentioned, the rotation matrix is not linearized on its angle parameter, however, due to the extra degree of freedom in the matrix it is possible to linearize up to the first term for the ray properties. This property is utilized in chapter 7, where a new $M$ matrix is created for a reflective grating.

Next to the definition of the ray vector, the method also addresses homogeneous points. These points in two-dimensional space are represented by a 3x1 vector as $P = [1, x, y]^T$. In the supplementary work published for the article from 2022 [7] it was stated that the cross-section of two rays is found by the cross-product of the two vectors. This algebraic benefit can be utilized for finding the placement of the ray on the detector. The algebraic definition of the cross-product of two rays is written as

$$P = \vec{r}_1 \times \vec{r}_2. \tag{4.6}$$

# 5
# Merit function

As discussed in chapter 2, a large set of optical requirements exist for the performance analysis of optical systems. For this research, it has been decided that the spot size and its location will be the first incorporated requirements for the analytical framework. This chapter discusses the calculation of the different merit functions and how it is incorporated within the analytical framework for the verification in chapter 6 and the use case in chapter 8.

## 5.1. Spot size

The spot size is measured over one axis since the analytical framework traces rays in one plane. The marginal rays originating from the source are traced and their relative difference in intersection on the image plane is set to be the spot size. Both marginal rays intersect the image plane the furthest from the chief ray, hence the spot value is categorized as the spot diameter. This is schematically represented in Figure 5.1.

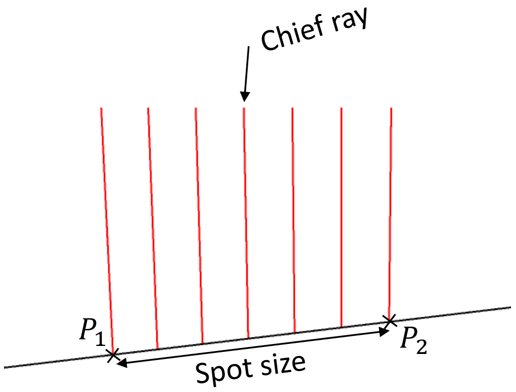

**Figure 5.1:** Schematic representation of the definition of spot size

The intersections with the image plane are obtained in the global coordinate system. Hence the spot size is defined as the Euclidean distance between the two intersection points. The formula for the Euclidean distance between two points consisting of an x and y coordinate is written as

$$f_{spot} = \sqrt{(x_2 - x_1)^2 + (y_2 - y_1)^2}. \tag{5.1}$$

To find the derivatives of Equation 5.1 and apply these in the sensitivity analysis of a system, the function is simplified to

$$f_{spot}(u,v) = \sqrt{u^2+v^2}, \tag{5.2}$$

where $u = x_2 - x_1$ and $v = y_2 - y_1$. From this simplified equation, the first and second-order derivatives are calculated by

$$\frac{\partial f}{\partial x_i} = \frac{u}{\sqrt{u^2+v^2}}\frac{\partial u}{\partial x_i} + \frac{v}{\sqrt{u^2+v^2}}\frac{\partial v}{\partial x_i}, \tag{5.3}$$

$$\frac{\partial^2 f}{\partial x_i^2} = \frac{1}{\sqrt{u^2+v^2}}\left(\frac{\partial^2 u}{\partial x_i^2} + \frac{\partial^2 v}{\partial x_i^2}\right) - \frac{u\frac{\partial^2 u}{\partial x_i^2} + v\frac{\partial^2 v}{\partial x_i^2}}{(u^2+v^2)^{3/2}}, \tag{5.4}$$

$$\frac{\partial^2 f}{\partial x_i \partial x_j} = \frac{1}{\sqrt{u^2+v^2}}\left(\frac{\partial^2 u}{\partial x_i \partial x_j} + \frac{\partial^2 v}{\partial x_i \partial x_j}\right) - \frac{u\frac{\partial^2 u}{\partial x_i \partial x_j} + v\frac{\partial^2 v}{\partial x_i \partial x_j}}{(u^2+v^2)^{3/2}}. \tag{5.5}$$

The intersection coordinates, $x_1, x_2, y_1, y_2$, of the ray with the detector plane are defined with Equation 4.6. The detector plane is set up as a vector, and the incoming ray is defined by all matrix multiplications that hold the orientation variables of the optical elements. As a result, the intersection is given within the framework as

$$P_1 = \vec{r}_d \times (M_{system}\vec{r}_1) = \begin{bmatrix} 1 \\ x_1 \\ y_1 \end{bmatrix}. \tag{5.6}$$

Where $\vec{r}_d$ is the vector of the detector plane, $M_{system}$ is the matrix that defines the optical system and $\vec{r}_1$ is the light ray originating from the source. $M_{system}$ is system-dependent and its structure and variables rely on the elements within the system, where each optical element is represented by Equation 4.5 and multiplied sequentially. As a result of Equation 5.6, the functions $u$ and $v$ in Equation 5.2 are found by

$$\begin{bmatrix} 0 \\ u \\ v \end{bmatrix} = P_2 - P_1. \tag{5.7}$$

If the optical system in Equation 5.6 is represented by one $M$ matrix, the derivatives on one intersection are found by

$$\begin{aligned} \frac{\partial P_1}{\partial x_i} =& \frac{\partial \vec{r}_d}{\partial x_i} \times (T \cdot R \cdot M \cdot R^{-1} \cdot T^{-1} \cdot \vec{r}_1) \\ &+ \vec{r}_d \times \left(\frac{\partial T}{\partial x_i} \cdot R \cdot M \cdot R^{-1} \cdot T^{-1} \cdot \vec{r}_1\right. \\ &+ T \cdot \frac{\partial R}{\partial x_i} \cdot M \cdot R^{-1} \cdot T^{-1} \cdot \vec{r}_1 \\ &+ T \cdot R \cdot \frac{\partial M}{\partial x_i} \cdot R^{-1} \cdot T^{-1} \cdot \vec{r}_1 \\ &+ T \cdot R \cdot M \cdot \frac{\partial R^{-1}}{\partial x_i} \cdot T^{-1} \cdot \vec{r}_1 \\ &\left.+ T \cdot R \cdot M \cdot R^{-1} \cdot \frac{\partial T^{-1}}{\partial x_i} \cdot \vec{r}_1\right). \end{aligned} \tag{5.8}$$

Where $x_i$ represents the variables present in the system to describe the placement and orientation of the optical elements. This derivation remains valid for larger-scale systems, where additional terms are incorporated, and an increased number of terms become zero because the placement variables of the first element are not present in the description for the placement of the second mirror.

Within the analytical framework, the spot size value is allowed to have a positive or negative sign. A minus sign for the spot size indicates that the light will be focused in front of the image plane, this reasoning results in a positive sign when the light is focused behind the image plane. The theory behind this formulation is to ensure a continuous function for the spot size since this is of importance in the nominal position. The construction of analytical sensitivities demands continuous functions that can be evaluated everywhere within the given domain.

This research will focus on the optical performance calculations by means of analyzing the spot size. For optimization of an optical system, the merit function should have a minimum or maximum for the set of variables. The construction of the merit function how it is used for the performance calculation, does not allow for optimization. If the merit function should be altered for optimization, the signed spot size should be squared to obtain a minimum, or maximum, in the sensitivities.

## 5.2. Location of spot

The location of the spot is defined as the distance between the center of the image plane, or detector, and the intersection of the chief ray with that plane. This intersection can be found by Equation 4.6 in the global coordinate frame, however, when both the rays are rotated and displaced into the local coordinate frame of the detector it simplifies the equation. The cross product of these vectors results in a coordinate where $y$ is zero, and the location on the detector is the $x$ coordinate. Since the location is the x coordinate, the second entry of the vector is found by

$$f_{location} = -(R_{\theta_d}^{-1} T_{u_d,v_d}^{-1} \vec{r}_d)_1 (R_{\theta_d}^{-1} T_{u_d,v_d}^{-1} M_{system} \vec{r}_{cr})_3 + (R_{\theta_d}^{-1} T_{u_d,v_d}^{-1} \vec{r}_d)_3 (R_{\theta_d}^{-1} T_{u_d,v_d}^{-1} M_{system} \vec{r}_{cr})_1. \tag{5.9}$$

In Equation 5.9, the chief ray, $\vec{r}_{cr}$, from the source is transformed by the optical system, $M_{system}$, and rotated and translated into the local coordinate frame of the detector $\vec{r}_d$. Throughout this research, optical performance is described as the spot size, only in Table 9.3 Equation 5.9 is used as the merit function.

## 5.3. Taylor expansion of the merit function

This section discusses the Taylor expansion used for the optical performance approximation for dynamic perturbated systems. The expansion is composed of the first- and second-order sensitivities of the merit function, which are obtained from the analytical framework as explained above and constructed in the Jacobian and Hessian matrices. These matrices are incorporated into the expansion of the merit function as

$$f(\tilde{x} + h) = f(\tilde{x}) + J_f(\tilde{x})h + \frac{1}{2}h^T H_f(\tilde{x})h. \tag{5.10}$$

In Equation 5.10, the spot size is calculated for the system whilst perturbed by the $h$ vector. This calculation is performed by incorporating the Jacobian ($J_f$) and Hessian ($H_f$) matrices, which are evaluated for the nominal position of the spectrometer, denoted by the $\tilde{x}$ vector. $\tilde{x}$ holds the values for the placement and orientation of all elements in the nominal position. Both the merit function for the spot size and the location of the spot can be interpreted for $f$. The products are added to the nominal merit function value to review the implied changes. This approximation is first applied in chapter 9 where the displacement field of a homogeneous expansion, gravity and vibrations is analyzed for a Czerny-Turner spectrometer.

# 6

# Model verification

In this chapter, the analytical framework will be compared to results in Zemax for a system that consists of two spherical off-axis mirrors. The three degrees of freedom of both mirrors are investigated in a parametric study, and later the sensitivities of these variables are constructed and examined. In this analysis, the studies for both the paraxial ray tracing and standard ray tracing in Zemax are included for verification.

## 6.1. Optical system

For the verification of the analytical framework, a simple model is used that consists of two spherical mirrors. Within the paraxial approximation, spherical mirrors focus collimated light into a perfect focus point. With this knowledge, two paraxial spherical mirrors can image a point perfectly as seen in Figure 6.1. The nominal values for the variables of the system can be seen in Table 6.1.

**Table 6.1:** Nominal values of variables in the system depicted in Figure 6.1. M1 is the collimating mirror of the system and M2 is the imaging mirror of the system.

| Parameter | Value | | Description |
|---|---|---|---|
| $\theta_{M1}$ | 30 | [deg] | Angle of M1 |
| $Q_{M1}$ | (5.7735, 0) | [mm] | Coordinates, M1 |
| $r_{M1}$ | 10 | [mm] | Radius of M1 |
| $\theta_{M2}$ | 30 | [deg] | Angle of M2 |
| $Q_{M2}$ | (0.7735, 8.6603) | [mm] | Coordinates, M2 |
| $r_{M2}$ | 10 | [mm] | Radius of M2 |

The first mirror collimates the light that originates from the point source which is in the left bottom of Figure 6.1 and is located at $(0, 0)$. The perfectly collimated light is imaged by the second spherical mirror onto the image plane. Both the object and image plane are set to the focus of both mirrors so that a perfect image is formed in the image plane. The perfect image has an infinitely small spot size, which is constructed when all rays cross the detector at the same location.

Rigid body displacements from the nominal position of both mirrors cause variations in the spot size. For example, when the first mirror is displaced toward the point source, the light bundle towards the imaging mirror becomes diverging instead of collimated. As a result, the focusing power of the second mirror is too weak and forms an imperfect image formation.

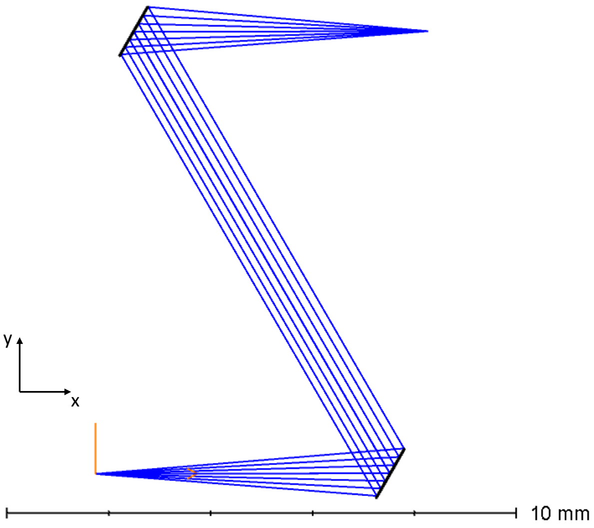

**Figure 6.1:** Optical design of verification model consisting of two spherical mirrors

## 6.2. Parametric study

The first step in the verification of the analytical sensitivities is a parametric study. Within this study, the merit function is evaluated for variations in every variable on a given bounded domain, for both the analytical framework and Zemax. When the results of the analytical framework show a great resemblance with the results in Zemax, it is a valid method for the calculation of the spot size. Moreover, the similarity also indicates that the sensitivities of the analytical framework are likely to coincide with the sensitivities of the verification model. Therefore, in this section, the parametric study of the simple model is discussed. The parametric study consists of changes in the in-plane placement and rotation of both mirrors. The change in location of the point source and image plane are not considered in this study.

The merit function is calculated in Figure 6.2 to Figure 6.7 by four different methods and indicated by different colors. The color blue is associated with the parametric study of the analytical framework. Second, the red color defines the study done in Zemax whilst the paraxial assumption is of effect. The last two methods are indicated by the color black and calculate the one-dimensional spot size in Zemax for the meridional and sagittal plane without paraxial approximation.

From all plots can be obtained that the results for the parametric study of both the analytical method and Zemax paraxial method strongly align. This result is most likely since both methods hold the same assumptions. Each variable will be discussed in more detail in the following section.

In Figure 6.2, the spot size is shown for varying x positions of the first mirror. Since the source is located in the exact focus of the first mirror, displacement of the first mirror over de x-axis causes the outgoing light to become non-collimated. The obtained results of the framework align with the Zemax paraxial analysis. The most interesting outlier for this variable is the YZ plane. The dashed line in the lower part of the figure shows a non-linear relation which is not suspected for a displacement of a mirror in a linear model. Since this result is obtained by standard ray tracing, the non-linear relation is most likely due to astigmatism and coma created by the tilted spherical mirrors.

For the displacement in y-direction for the first mirror, all methods show functions close to linear, as seen in Figure 6.3. Due to a positive displacement over the y-axis, the incoming light travels a distance shorter than the focal length to the first mirror. This causes the collimated light to become divergent, and therefore a larger spot size on the detector is observed. Moreover, the sign of all methods is the same, only the analysis for the YZ plane knows a large offset. This is due to the astigmatism created by tilted spherical mirrors.

In Figure 6.4, the effect on spot size for the rotation of the first mirror is presented. The rotation matrix in the matrix formulation holds a non-linear relation to describe the orientation of the optical elements. This non-linearity can be seen in the figure for both the analysis in Zemax and the analytical framework. For the different analyzed planes in the standard Zemax analysis, the XZ plane shows a convex relation between the spot size and its rotation. However, the YZ plane does not possess this function.

The same conclusions found for the x position of the first mirror also account for the results found in Figure 6.5. The sign is the only difference between the two analyses, which is expected since the displacement of the complete system in the same direction does not change the optical performance. Since the light source and detector plane remain fixed in the x position in this analysis, the magnitude of the first-order sensitivities is not equal.

The parametric study of both the analytical framework and the paraxial Zemax analysis shows that the y position of the second mirror has little impact on the spot size. The cause of this is that ray aiming is disabled in both analyses, which causes the optical elements to grow in surface area when incoming rays can not be reflected due to the induced displacement. Due to this, the second mirror is always able to focus all light rays onto the detector plane while displaced over the y-axis. The location of the spot on the detector is not taken into account in this chapter, however, the displacement in the y-axis of the second mirror will have a linear relation toward the location of the spot on the detector.

In Figure 6.7, it can be seen that the sign for the paraxial analysis of the system counters the sign of the paraxial analysis in Figure 6.4. This result is as expected, however the same does not hold for the analysis on the YZ plane in Zemax. The nominal position of the mirrors in the paraxial design is not the optimal position for the spot size in the YZ plane for a standard Zemax analysis. Due to this, the parametric study for the rotation of the two mirrors shows the same sign for the first-order sensitivity in the nominal position instead of the contrary sign.

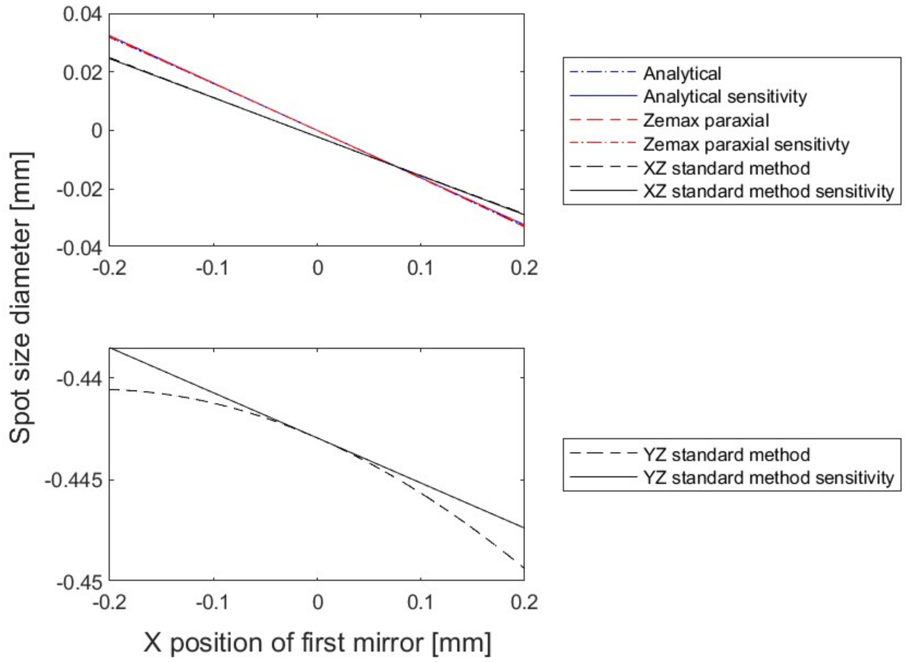

**Figure 6.2:** Parametric study on the X position of the first mirror, and the sensitivity found in the nominal position by different computation methods

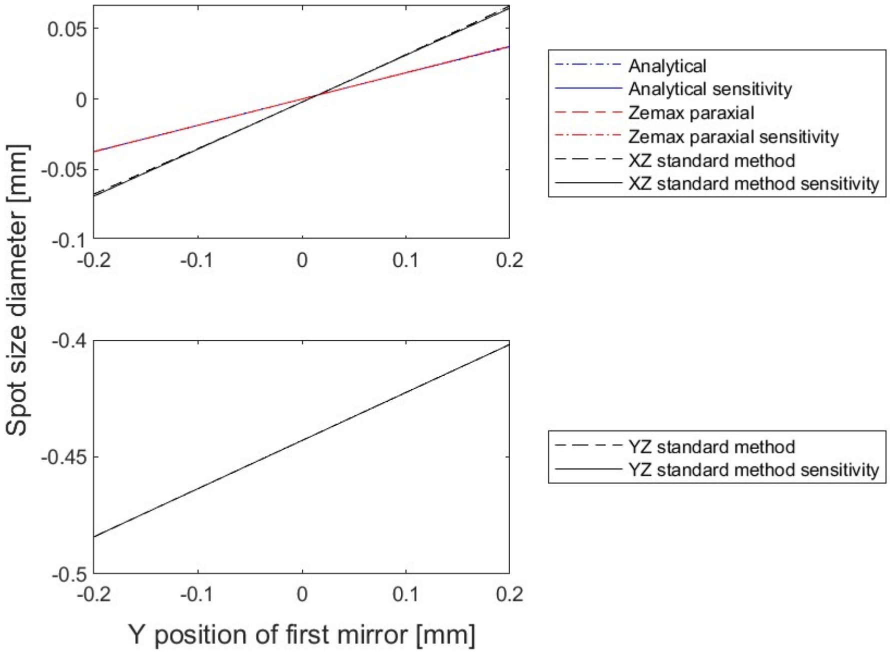

**Figure 6.3:** Parametric study on the Y position of the first mirror, and the sensitivity found in the nominal position by different computation methods

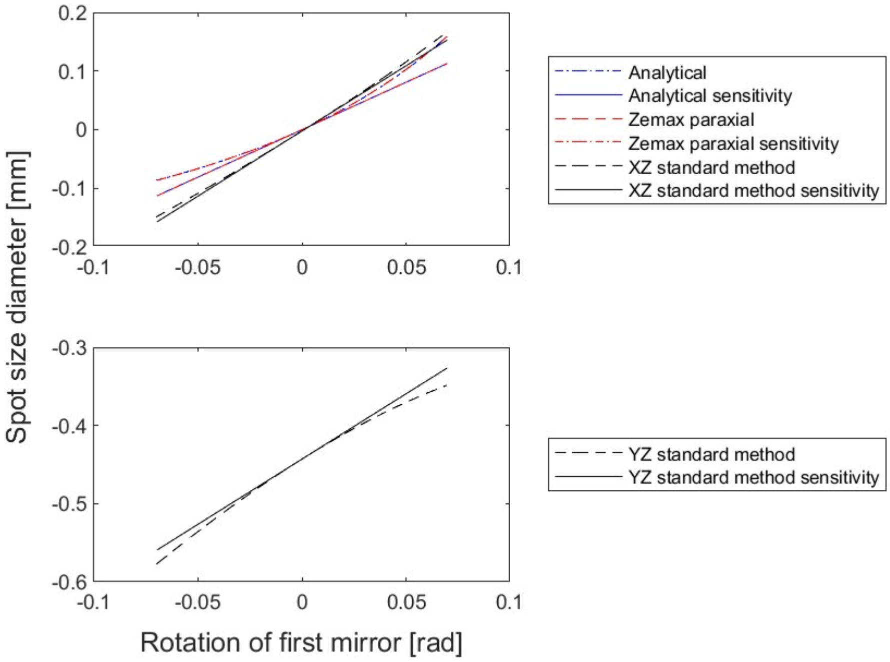

**Figure 6.4:** Parametric study on the rotation angle of the first mirror, and the sensitivity found in the nominal position by different computation methods

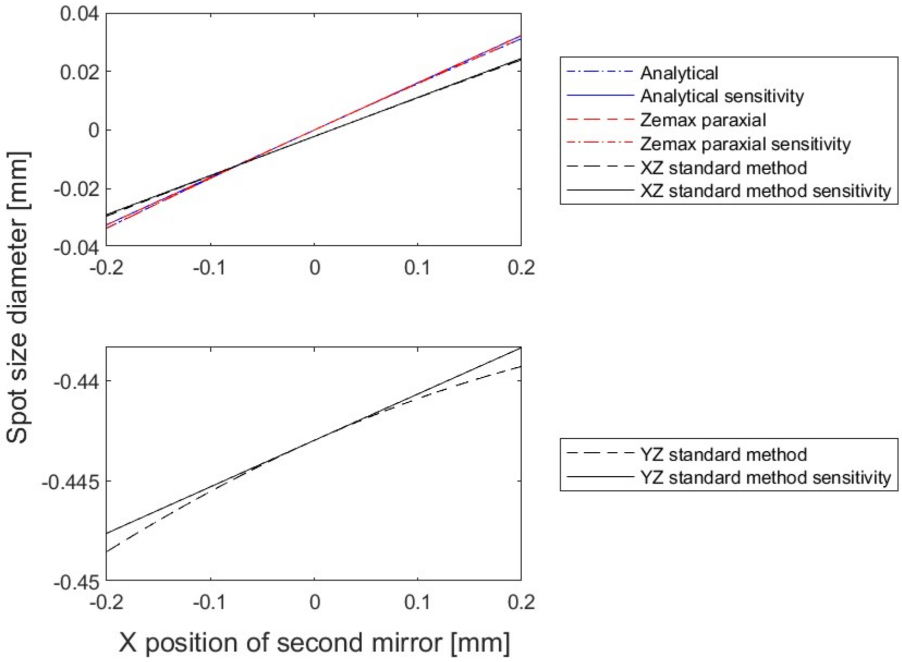

**Figure 6.5:** Parametric study on the X position of the second mirror, and the sensitivity found in the nominal position by different computation methods

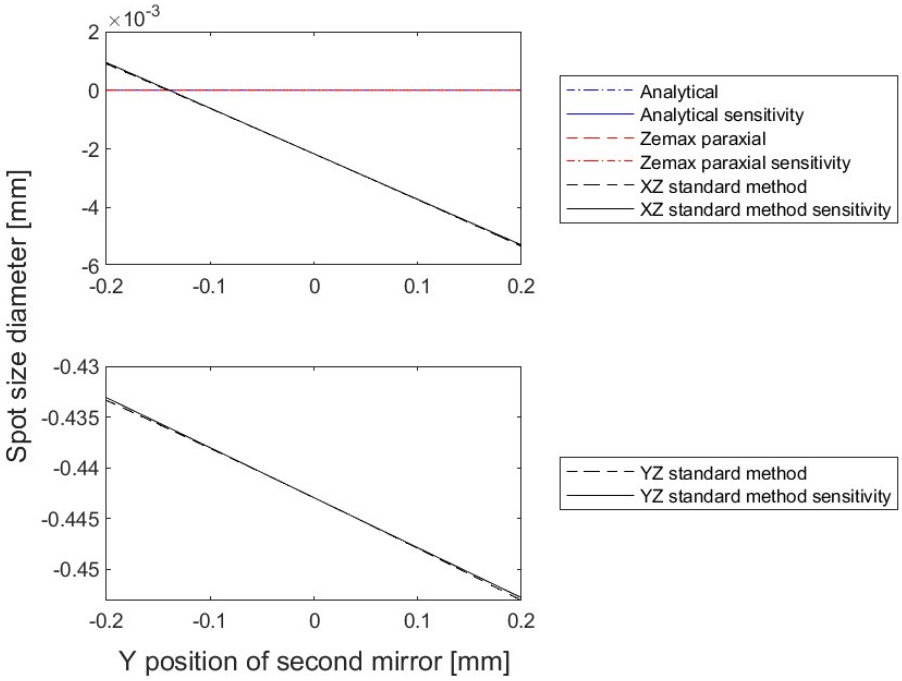

**Figure 6.6:** Parametric study on the Y position of the second mirror, and the sensitivity found in the nominal position by different computation methods

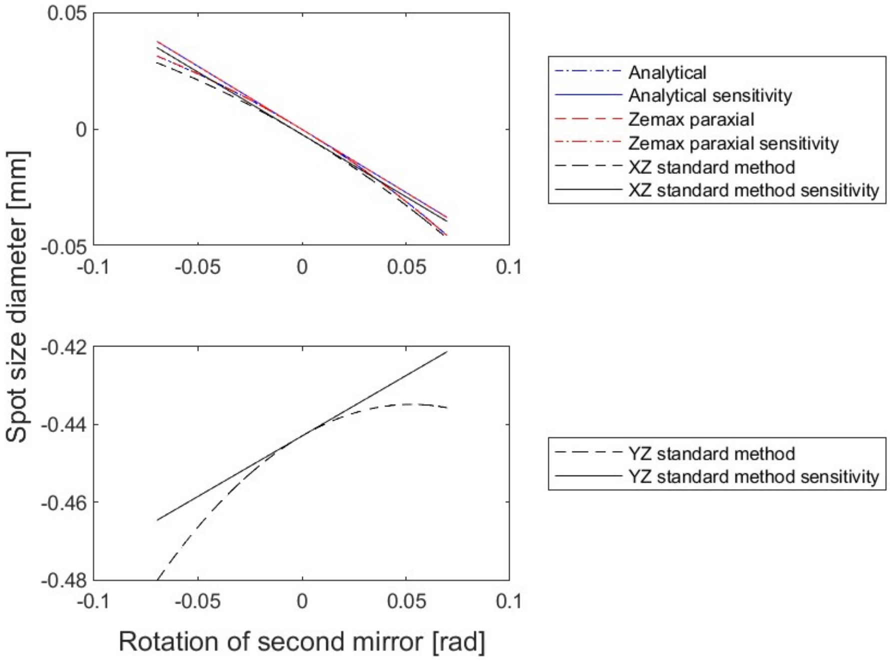

**Figure 6.7:** Parametric study on the rotation angle of the second mirror, and the sensitivity found in the nominal position by different computation methods

From the parametric studies, it is concluded that the results of the analytical proposed method closely resemble the results from Zemax using the paraxial approximation. For further investigation on the overlap, the absolute difference between both methods for the rotation on the first mirror is plotted in Figure 6.8, since this variable holds the largest difference. The plots for all other variables can be found in Appendix B.

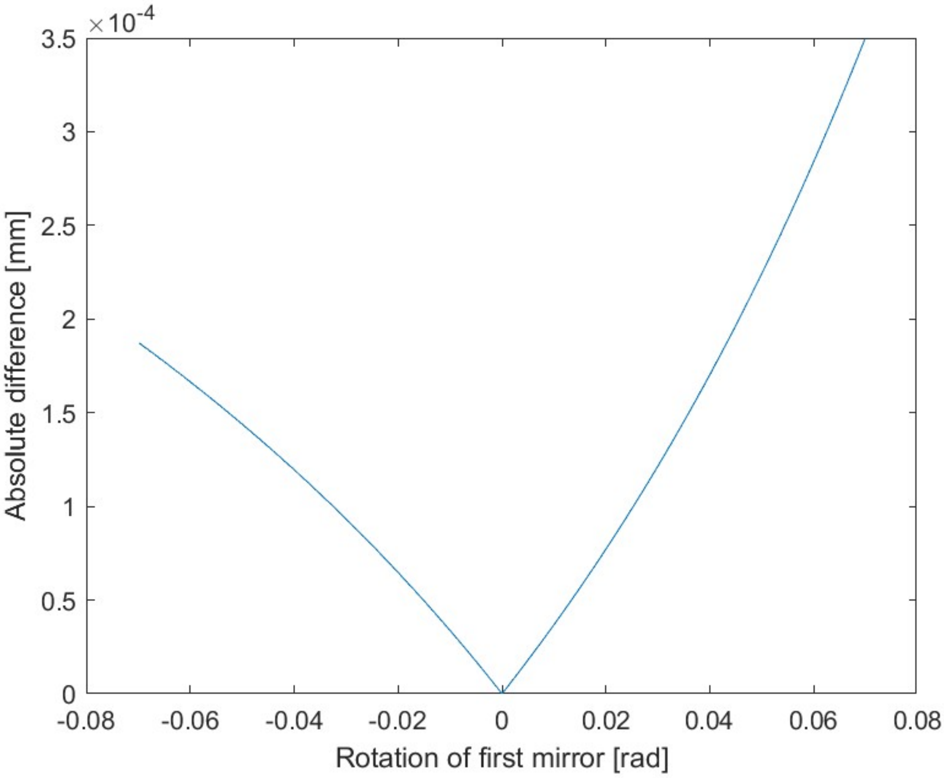

**Figure 6.8:** Absolute difference on spot size for the parametric study of the rotation of the first mirror in Zemax and analytical framework

The order of the absolute difference for the rotation of the first mirror is at maximum $10^{-4}$mm. This order of magnitude is also found for the rotation of the second mirror, while the order for the other variables is lower. This is of importance for both the accuracy of the analytical method and a sanity check for the verification of the sensitivities found via the analytical framework. Due to the small differences between the analytical framework and paraxial analysis in Zemax, it can be concluded that the analytical framework is valid for optical systems designed with paraxial approximation.

## 6.3. Sensitivities table

This section discusses the retrieval of the first-order sensitivities, using Zemax and the proposed method to calculate the optical performance, and goes into depth about the differences and their significance. The first-order sensitivities include only the slope at a given degree of freedom. Therefore, the first-order sensitivities in the nominal position are mentioned as slopes and reviewed in this section. First, the verification of the derivation of the analytical merit function is checked by finite differencing and later the obtained sensitivities are compared with Zemax.

### Step size in finite differencing

To verify the accuracy of the analytically obtained sensitivities, the results are compared with the sensitivities obtained by the analytical framework with central finite differencing. The absolute value of the relative difference between analytical and finite differencing should be lower than the maximum error in Figure 6.8. The difference between both derivation methods is plotted for different step sizes and each variable to determine a suitable step size. The results for this can be found in Appendix B. The concluding step sizes for each variable are in Table 6.2. The step size found for the y displacement of the second mirror is much larger due to the small relative difference between both calculation methods. The relative difference for this sensitivity is in the order of $10^{-11}$ which causes the step size of $10^{-10}$ to not account for the truncation error.

Via this method, the truncation error of the sensitivities can be determined for finite differencing, and the corresponding step size is found for accurate derivatives. Moreover, the sensitivities from Zemax are obtained with finite differencing, and the step sizes found in the relative difference plots are used as a reference frame for this retrieval. However, the small step size of $10^{-10}$ resulted in unclear results due to noise for the tolerancing analysis in Zemax, hence the larger step size of $10^{-5}$ was used for the finite differencing of all variables in Zemax.

**Table 6.2:** Different step sizes for central differencing on all degrees of freedom

| Degree of Freedom | | Step size |
|---|---|---|
| x-displacement first mirror | (xM1) | $10^{-10}$ |
| y-displacement first mirror | (yM1) | $10^{-10}$ |
| Rotation first mirror | (rM1) | $10^{-10}$ |
| x-displacement second mirror | (xM2) | $10^{-10}$ |
| y-displacement second mirror | (yM2) | $10^{-5}$ |
| Rotation second mirror | (rM2) | $10^{-10}$ |

## Sensitivities table

This section discusses the first-order sensitivities as seen in Figure 6.2 to Figure 6.7. The differences and relevance of the multiple lines are explained and an overall conclusion on the obtained sensitivities is drawn.

The YZ-plane in Zemax corresponds with the plane that the analytical framework is investigating, which is also the plane depicted in Figure 6.1. Due to the introduction of off-axis spherical mirrors, the system suffers from astigmatism and coma when the paraxial approximation is neglected. The different spot sizes found for the YZ and XZ planes, whilst not using the paraxial approximation, are mainly caused by astigmatism.

The color scheme for the sensitivities is the same as for the parametric study, and only for the Zemax paraxial sensitivity the line structure is a dash-dot line. It can be seen in the figures that the sensitivities of the analytical method strongly correlate with Zemax paraxial analysis. Next to this, the slope of the XZ standard method holds for every variable the same sign in comparison with the paraxial analysis. Moreover, the sensitivities can be seen in Table 6.3 with the relative difference between the first-order derivatives in Table 6.4.

**Table 6.3:** First-order sensitivities found by all methods on each system variable

| | Analytical | Numerical | | | |
|---|---|---|---|---|---|
| | Corcovilos | Zemax par | Zemax standard XZ-plane | Zemax standard YZ-plane | Corcovilos |
| xM1 | -0.1616 | -0.1619 | -0.1334 | -0.0221 | -0.1616 |
| yM1 | -0.1865 | -0.1870 | 0.3335 | 0.2054 | -0.1865 |
| rM1 | 1.6155 | 1.6191 | 2.2213 | 1.6685 | 1.6155 |
| xM2 | 0.1616 | 0.1619 | 0.1333 | 0.0231 | 0.1616 |
| yM2 | 0.0000 | 0.0000 | -0.0156 | -0.0492 | 0.0000 |
| rM2 | -0.5385 | -0.5397 | -0.5319 | 0.3105 | -0.5385 |

The difference between the sensitivities of the analytical framework and Zemax paraxial analysis is in the order of $10^{-3}$ or smaller for all variables. The differences in the standard analysis in Zemax for the two planes show that there is no comprehensive conclusion for the usage of the analytical sensitivities in an optical performance calculation. For systems to be analyzed without the paraxial approximation, the analytical sensitivities fall short.

The sensitivities for both the angles of the mirrors can be seen to be larger in comparison to the displacement sensitivities. This phenomenon is described by Lindlein *et al.* [25] as that a widely opened parabolic mirror, which the spherical mirror approximates, is very sensitive to slight off-axis incoming light. Hence the sensitivities are confirmed to follow previously established knowledge about sensitivities of mirrors. Furthermore, the rotation of the first mirror proposes a larger error since the error

**Table 6.4:** Difference between all methods with analytical framework for the first-order sensitivities

| | Corcovilos - Zemax paraxial | Corcovilos - Zemax XZ-plane | Corcovilos - Zemax YZ-plane |
|---|---|---|---|
| xM1 | 3.48E-04 | 2.81E-02 | 1.39E-01 |
| yM1 | 4.06E-04 | 5.20E-01 | 3.92E-01 |
| rM1 | 3.54E-03 | 6.06E-01 | 5.30E-02 |
| xM2 | 3.48E-04 | 2.82E-02 | 1.38E-01 |
| yM2 | 5.25E-11 | 1.56E-02 | 4.92E-02 |
| rM2 | 1.17E-03 | 6.62E-03 | 8.49E-01 |

propagates through the system for a longer distance. Again, the same results are found for the paraxial analysis in Zemax.

Moreover, the sensitivities of the first mirror are in an absolute sense all larger than the sensitivities of the second mirror. The error on the spot size induced by these alterations propagates through the system for a longer distance in comparison to the second mirror. Hence have a larger effect on the spot size.

The error percentage of the analytical sensitivities to the Zemax paraxial sensitivities are all within $0.2 - 0.25\%$. From this, it is concluded that the accuracy of the analytical sensitivities is sufficient for the purpose of this research. The sensitivities will be used on a dynamically perturbed system, and the optical performance over time is the final outcome. This outcome will include both the first and second-order sensitivities, with additional cross-dependencies. Therefore, the $0.2 - 0.25\%$ error on the sensitivities is sufficient.

# 7

# Modeling of grating

This chapter discusses the modeling of a grating within the analytical framework verified in chapter 6. The formulation of Corcovilos focuses on simple optical elements, and this chapter delves into modeling a more complex element within the framework. In general, the grating is used in optical systems for the dispersion of the incoming spectrum. The practical applications of this property are, for example, investigating the percentage of one wavelength in a spectrum and using the grating as a wavelength selector. The content of this chapter centers first around the controls that adjust the performance of a grating. Second, the grating's performance is examined through both the analytical grating and a numerical investigation in Zemax.

## 7.1. Theory of grating

The grating is applied in optical systems for the dispersion of light. The amount of dispersion is dependent on the different wavelengths within the spectrum of the incoming light, the spacing between lines, and the angle under which the incoming light hits the grating. Dispersion via grating is achieved by transmission or reflection of the light, for this research only the reflective grating will be considered. This section will discuss the variables a grating holds and the effect on spectral resolution.

Figure 7.1 schematically shows the incoming and outgoing light rays at the surface of a grating and its variables. The angular dispersion can be derived from the outgoing angle of the light when differentiated to wavelength. The variables shown in Figure 7.1 describe the performance of a grating in the following formula

$$k\lambda = d(sin(\beta) - sin(\alpha)). \tag{7.1}$$

For this equation, $k$ is the diffraction order of interest for the analysis. The constructive and destructive property of light as a wave shows that for different orders, the angle of the outgoing light from the grating becomes different. The spacing between the grating lines is given by $d$. Smaller values of $d$ result in a larger angular dispersion of the light, however, the value of $d$ has a physical limit since the lines can not be infinitely close due to manufacturability. The unit of $d$ is $\mu$m per line. The different wavelength, or spectrum, of the incoming light is represented by $\lambda$ in Equation 7.1. Moreover, the equation also shows that the outgoing angle, $\beta$, of the light is dependent on the angle of the incoming light. This property will be utilized for the modeling of the grating for the analytical framework.

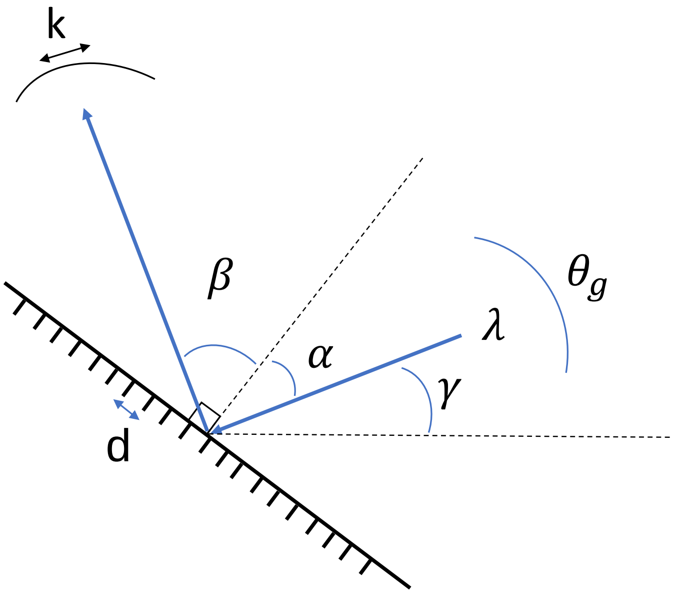

**Figure 7.1:** Schematic representation of grating presented with its variables

## 7.2. Modeling of grating

The matrix method of Corcovilos does not elaborate on the modeling of reflective gratings. For the use case of the Czerny-Turner spectrometer, a grating is needed. Therefore, in this section, the modeling of a reflective grating is introduced.

Equation 7.1 is written as a function of the angles of the incoming and reflected ray. Since the formulation of Corcovilos describes rays with slope instead of angle, this function is rewritten to

$$m_o = tan(asin(sin(atan(m_i)) + \frac{kl}{d})), \tag{7.2}$$

where $m_o$ is the slope of the reflected ray in the gratings local coordinate system and $m_i$ is the slope of the incoming ray. Moreover, the relation of $m_i$ is given by $tan(\theta_g - \gamma)$, where $\gamma$ represents the angle of the incoming ray in the global coordinate system with respect to the gratings normal and $\theta_g$ is the nominal angle of the grating as seen in Figure 7.1. The variable $k$ in Equation 7.2 represents the diffraction order of the grating, throughout this research only the first order is of interest, hence from here on it is set to 1. Unfortunately, Equation 7.2 does not allow for a linear operation for the slope on the incoming ray. However, due to the extra degree of freedom inside the matrix formulation a linearization can be implemented to create a linear operation. For this, the chief ray is used as the linearization point, which is indicated by $\bar{m}_i$. The first derivative of $m_o$ to $\bar{m}_i$ is found when Equation 7.2 is expressed with $\bar{m}_i$ instead of $m_i$, and results in

$$\frac{\partial m_o}{\partial \bar{m}_i} = \frac{\left(\frac{1}{\sqrt{\bar{m}_i^2+1}} - \frac{\bar{m}_i^2}{(\bar{m}_i^2+1)^{3/2}}\right)}{\sqrt{1 - \left(\frac{\bar{m}_i}{\sqrt{\bar{m}_i^2+1}} + \frac{l}{d}\right)^2}} + \frac{\left(\frac{\bar{m}_i}{\sqrt{\bar{m}_i^2+1}} + \frac{l}{d}\right)^2 \left(\frac{1}{\sqrt{\bar{m}_i^2+1}} - \frac{\bar{m}_i^2}{(\bar{m}_i^2+1)^{3/2}}\right)}{\left(1 - \left(\frac{\bar{m}_i}{\sqrt{\bar{m}_i^2+1}} + \frac{l}{d}\right)^2\right)^{3/2}}. \tag{7.3}$$

The linearization at the chief ray allows for the incorporation of converging and diverging light beams onto the grating and the creation of a linear operation. The relative difference between the slope of the marginal rays and the chief ray cannot decrease for a different input, hence the introduced error in the linearization is smallest when the slope of the chief ray is used for the point of linearization. Next to this, a grating is mostly employed in a system where collimated light propagates to the grating. Therefore the assumption for a linearization around the chief ray is set valid. This linear operation is included as

$$m_o = a - b(m_i - \bar{m}_i), \tag{7.4}$$

where $m_i$ is the slope of the incoming ray and $\bar{m}_i$ the slope of the chief ray. Moreover, $a$ is Equation 7.2, and $b$ is Equation 7.3. This linearization is integrated within a new $M$ matrix as

$$\begin{bmatrix} h_o \\ m_o \\ 1 \end{bmatrix} = \begin{bmatrix} -1 & 0 & 0 \\ 0 & b & a - (b \cdot \bar{m}_i) \\ 0 & 0 & -1 \end{bmatrix} \begin{bmatrix} h_i \\ m_i \\ 1 \end{bmatrix}. \tag{7.5}$$

## 7.3. Verification of grating

In order to verify the analytical model numerically, a single grating is simulated in Zemax. This section delves into the model itself and the findings from both grating models.

The model consists of a grating placed perpendicular to the optical axis, which is placed on the x-axis. For the grating, the diffraction order is set to 1 and the grating constant, $d$, is set to 1.67 $\mu$m per line. The detector in the model is the y-axis, so the y-coordinate of each wavelength on $x = 0$ is of interest. These values were obtained by both the analytical model and Zemax for the verification of the analytical performance. The angle, $\alpha$, of the polychromatic light hitting the grating is set to 10 degrees. Moreover, the spectrum range of the polychromatic light is 550-850 nm and is simulated by 21 deterministic rays. This setup is schematically shown in Figure 7.2.

### Results

This section discusses the results found for the verification of the analytical model of the grating. The rays traced by the analytical grating are shown in Figure 7.2, where the grating is placed 1 mm in front of the source.

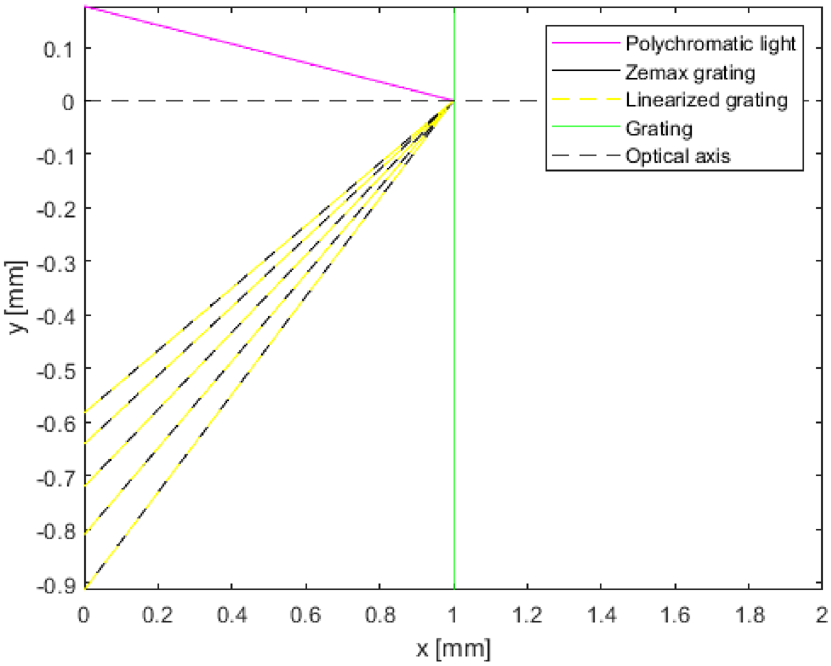

**Figure 7.2:** Grating modeled with incoming light and reflected dispersed light rays for grating in Zemax and linearized grating

The y-coordinates of the traced rays by the analytical framework can be reviewed in Figure 7.3. In the plot, the y-coordinates of the grating in Zemax are presented for verification. It can be concluded that both methods overlap greatly and an extra examination of the error has been conducted. The relative difference of both methods is found to be in the order of $10^{-16}$mm.

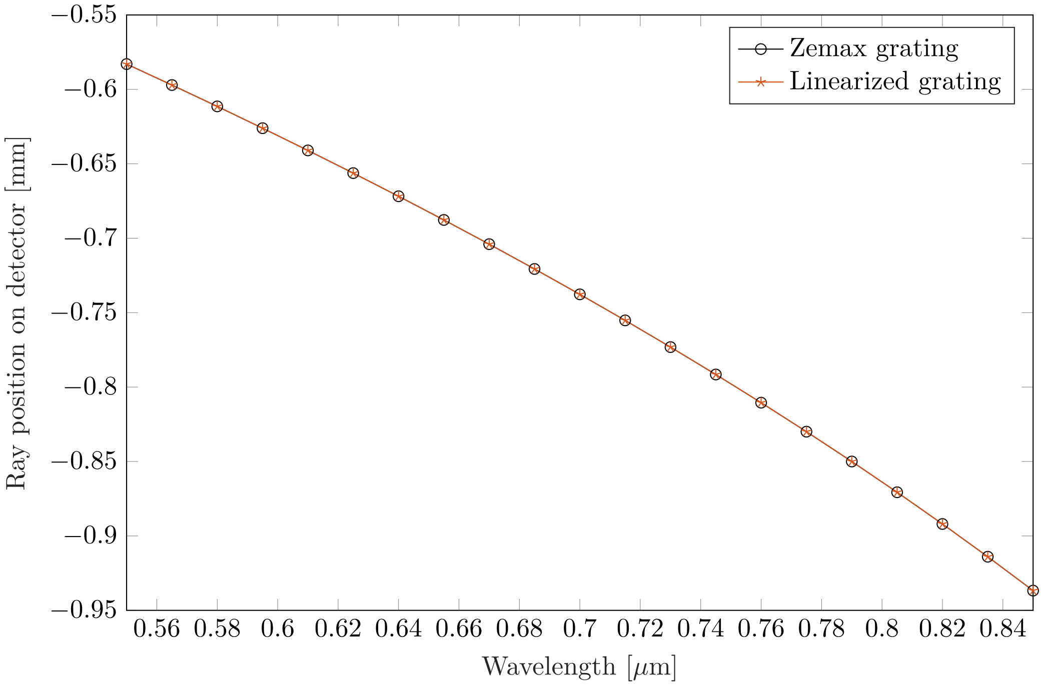

**Figure 7.3:** Y-coordinates of rays with different wavelengths on the detector for both Zemax and analytical model

It can be seen in Figure 7.3 that the different wavelengths are detected on the same y-coordinate on the detector. The difference between the analytical model of the grating and the corresponding numerical values is negligible. The values of the error are over the whole tested spectrum close to the floating-point accuracy, hence it is concluded that the analytical model is deemed suitable for implementation.

# 8

# Czerny-Turner Spectrometer

This chapter focuses on implementing the method by Corcovilos including the grating model introduced in chapter 7 for a Czerny-Turner spectrometer and finding the sensitivities of a more advanced optical system. Again, all results found by the analytical framework are compared with those obtained by the paraxial Zemax model. First, the layout of the Czerny-Turner model is discussed and the optical performance in the nominal position is computed by the analytical framework and paraxial Zemax model. Second, the sensitivities of both methods are compared and the established errors with Zemax are pointed out.

## 8.1. Model

The Czerny-Turner spectrometer consists of a slit, two spherical mirrors, and a grating before the dispersed light hits the detector. This set-up is widely used, with numerous articles published that go into depth about the possible dimensions [29]. Within the application gallery of Comsol, a Czerny-Turner Monochromator is analyzed for spectral resolution, and its dimensions are well documented [6]. It was decided to use this model for the use case of the analytical framework, with the benefit of easily obtaining displacement information of optical elements since the model already exists in FEM software. The remaining part of this section will elaborate on the specifics of the model and its dimensions.

In the spectrometer, the spectrum that is investigated enters the systems via the slit. From there, the light propagates with a Numerical Aperture (NA) of 0.05 toward the first spherical mirror. This mirror collimates the incoming light that propagates toward the grating. The grating reflects the different wavelengths with their respective angle, and the last spherical mirror focuses the light onto the detector. This optical system is represented in Figure 8.1.

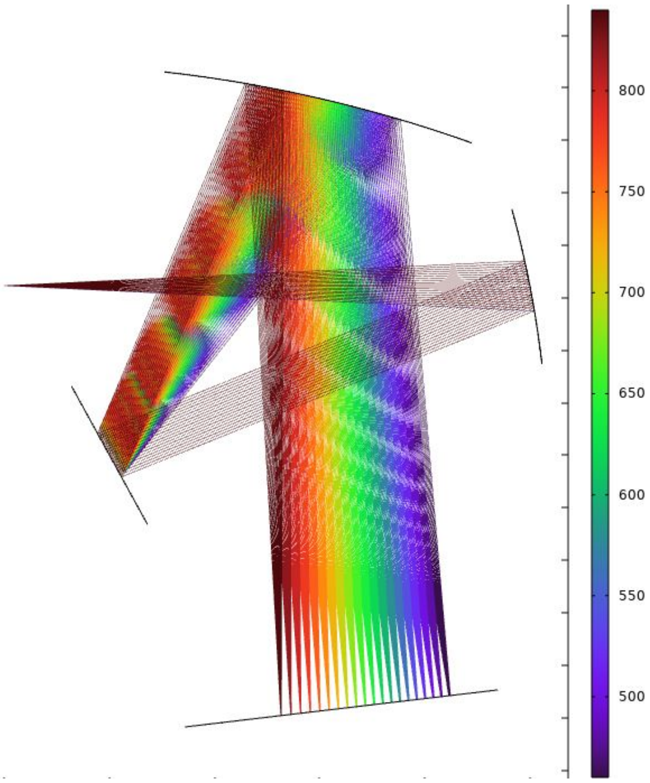

**Figure 8.1:** Spectrometer in Comsol from its application gallery

The optical performance is calculated in Comsol with the ray tracing module, however, this module does not allow systems to be evaluated with the paraxial approximation. Therefore, to verify the sensitivities of the analytical model, the spectrometer is also created in Zemax. For this, a coordinate change was implemented. The origin of the global coordinate system in Comsol is located in the center of the grating, where both Zemax and the analytical framework use the slit as its origin. The new coordinates of the optical elements and the used variables for the mirrors and gratings can be seen in Table 8.1.

**Table 8.1:** Numerical values of all variables in the Czerny-Turner Spectrometer

| Parameter | Value | Unit | Description |
|---|---|---|---|
| $\theta_g$ | 28.76 | [deg] | Grating's angle |
| $\theta_c$ | 11.0 | [deg] | M1's mirror |
| $\theta_i$ | 77 | [deg] | M2's mirror |
| $\theta_d$ | 6.76 | [deg] | Detector's angle |
| $Q_g$ | (10.00, -16.161) | [mm] | Coordinates, grating |
| $Q_c$ | (50.00, 0) | [mm] | Coordinates, M1 |
| $Q_i$ | (30.00, 17.84) | [mm] | Coordinates, M2 |
| $Q_d$ | (32.08, -40.28) | [mm] | Coordinates, detector |
| $R_c$ | 100 | [mm] | Radius M1 |
| $R_i$ | 130 | [mm] | Radius M2 |
| $d$ | 5/3 | [$\mu$m/lines] | Grating's constant |
| $k$ | 1 | - | Diffraction order |

Important to note is that the analytical framework defines angles anti-clockwise and Zemax clockwise to the global y-axis. Moreover, Zemax uses [lines/$\mu$m] as the unit for the grating's constant whereas the analytical framework uses the inverse of this as the unit. All values in Table 8.1 are given in the correct unit and coordinate frame for the analytical framework.

To verify if each variable from Table 8.1 is set correctly, the spot size in the nominal position is evaluated. The results of this are given for the three different wavelengths that are summarized in Table 8.2.

**Table 8.2:** Value of spot size for each wavelength in nominal position

| $\lambda$ [$\mu m$] | Analytical framework [$mm$] | Zemax [$mm$] | Relative error percentage [%] |
|---|---|---|---|
| 0.550 | 0.9418 | 0.9411 | 0.0722 |
| 0.700 | 0.7345 | 0.7338 | 0.1018 |
| 0.850 | 0.5506 | 0.5497 | 0.1543 |

From Table 8.2, it is concluded that the error, between both methods, on the spot size is sufficiently small and that each variable is set correctly. Next to this, for the different wavelengths the error between both methods is different. This wavelength-dependent error is introduced by the grating which is the only element that consists of a wavelength-dependent function. The error is concluded to be the cause of the linearization of the grating. In the linearization for the grating, only the angle of the incoming light is linearized and not the value for the wavelength. Since the reflection angle of the grating is also a function of the wavelength, the performed linearization introduces a wavelength-dependent error. The exact quantification of this error is a recommendation for further research.

## 8.2. Sensitivities

This section finds the sensitivities for the rigid body displacements and rotation of the two spherical mirrors, the grating, and the detector. As discussed in chapter 2, it is assumed throughout the research that all optical elements are rigid, so changes in the radius of mirrors are not taken into account. However, for the thermal disturbance discussed in chapter 9, the sensitivities on the radius are also found. The sensitivities on the rigid body displacement for the different wavelengths can be reviewed in Table 8.3 to Table 8.5.

The sensitivities obtained from Zemax are generated via the ZOS-API interface extension [38] in Zemax. This interface can seamlessly control the values within the lens data tab of a Zemax file and allows the user to let the results be calculated by the Zemax raytracer but controlled by a known scripting language. In this research, Python was used to set up the connection with Zemax and extract the generated values for the merit function.

The first conclusion for the sensitivities is based on the sign of the slope. For all variables, the slope has the same direction in comparison to the result found in Zemax. Therefore, when a variable is perturbed, the contraction or expansion of the spot size is consistently modeled by the analytical framework.

The size of the effect on the spot size depends on the magnitude of the slopes. The difference between the magnitudes of both methods is expressed as an error percentage, where the analytical value is taken as the measured value, and Zemax as the true value. These percentages can be found in the most right column of Table 8.3 to Table 8.5. The error percentage for most variables on all wavelengths is between $0.02 - 1.1\%$, with two outliers on both sides of this domain. The x displacement of the first mirror for $\lambda = 0.550$ has an extremely small error percentage of $0.0076\%$, and the sensitivity on the angle of the detector is out of proportion for $\lambda = 0.700$, which has an error percentage of $3.36\%$. The small error percentage does not hold any risk in the analysis, and fortunately, the larger error percentage on the angle of the detector will not have much impact due to the small magnitude of the respective sensitivity. However, further research may be implemented to investigate the origin of this error.

**Table 8.3:** Sensitivities found by the analytical framework and Zemax with their respective error percentages for $\lambda = 0.550\mu m$

| | Variable | Analytical | Zemax | Error percentage |
|---|---|---|---|---|
| Collimating mirror M1 | X | -0.13795 | -0.13794 | 0.00764 |
| | Y | -0.07533 | -0.07606 | 0.96559 |
| | $\theta_c$ | -0.12037 | -0.12167 | 1.06830 |
| Grating | X | 0.00400 | 0.00400 | 0.01388 |
| | Y | 0.00220 | 0.00220 | 0.01391 |
| | $\theta_g$ | 0.07276 | 0.07341 | 0.88204 |
| Imaging mirror M2 | X | 0.00038 | 0.00039 | 1.90841 |
| | Y | -0.06060 | -0.06065 | 0.06918 |
| | $\theta_i$ | -0.02296 | -0.02300 | 0.14859 |
| Detector plane | X | -0.00785 | -0.00785 | 0.04835 |
| | Y | 0.06621 | 0.06624 | 0.04835 |
| | $\theta_d$ | -0.00857 | -0.00853 | 0.45261 |

**Table 8.4:** Sensitivities found by the analytical framework and Zemax with their respective error percentages for $\lambda = 0.700\mu m$

| | | Analytical | Zemax | Error percentage |
|---|---|---|---|---|
| Collimating mirror M1 | X | -0.14250 | -0.14248 | 0.01900 |
| | Y | -0.06994 | -0.07063 | 0.97094 |
| | $\theta_c$ | -0.10770 | -0.10892 | 1.11585 |
| Grating | X | 0.00348 | 0.00348 | 0.02818 |
| | Y | 0.00191 | 0.00191 | 0.02820 |
| | $\theta_g$ | 0.06279 | 0.06340 | 0.96363 |
| Imaging mirror M2 | X | 0.00142 | 0.00143 | 0.56595 |
| | Y | -0.05852 | -0.05856 | 0.06080 |
| | $\theta_i$ | -0.02593 | -0.02598 | 0.16193 |
| Detector plane | X | -0.00736 | -0.00737 | 0.04382 |
| | Y | 0.06213 | 0.06215 | 0.04382 |
| | $\theta_d$ | -0.00129 | -0.00125 | 3.35745 |

**Table 8.5:** Sensitivities found by the analytical framework and Zemax with their respective error percentages for $\lambda = 0.850\mu m$

| | | Analytical | Zemax | Error percentage |
|---|---|---|---|---|
| Collimating mirror M1 | X | -0.15340 | -0.15335 | 0.03775 |
| | Y | -0.06677 | -0.06743 | 0.98181 |
| | $\theta_c$ | -0.09814 | -0.09932 | 1.18545 |
| Grating | X | 0.00282 | 0.00282 | 0.09311 |
| | Y | 0.00155 | 0.00155 | 0.09310 |
| | $\theta_g$ | 0.05477 | 0.05537 | 1.08059 |
| Imaging mirror M2 | X | 0.00238 | 0.00239 | 0.36919 |
| | Y | -0.05558 | -0.05560 | 0.05033 |
| | $\theta_i$ | -0.02953 | -0.02958 | 0.16714 |
| Detector plane | X | -0.00684 | -0.00684 | 0.03636 |
| | Y | 0.05767 | 0.05769 | 0.03636 |
| | $\theta_d$ | 0.00553 | 0.00557 | 0.81640 |

As outlined in chapter 6, the sensitivities of the initial mirror have a larger magnitude in comparison to subsequent elements. At the initial stages of the instrument, displacement causes a greater impact on the performance than displacement of the second mirror, this is due to the error being propagated over a longer distance.

Collimating and bringing the light into focus is for both the first and second mirrors respectively the most crucial. The placement along the axis on which the direction of the light is altered is more crucial for both mirror elements. This difference in sensitivity is inherent since the angles of the mirrors with respect to the optical axis of the incoming light are smaller than in the earlier verification model. The same line of reasoning holds for the displacement in y for the detector. The incoming light onto the detector has a small angle with the normal of the detector, thereby the sensitivity on the y placement becomes more important than the angle sensitivity for the detector.

From the sensitivities presented by the analytical framework, the conclusion is drawn that the accuracy is as desired. The grating adds a small wavelength-dependent error, which is the result of the linearization of the grating reflection angle formula. The quantification of this error is recommended for further research. To conclude this chapter, these findings support the robustness and reliability of the analytical model, creating a foundation for the incorporation of second-order derivatives and further research into perturbations.

# 9

# Optical performance calculation of dynamic model

As explored in chapter 5, the analytical framework demonstrates its computational strength when its sensitivities are applied to a Taylor expansion for the calculation of the optical performance. The retrieved sensitivities of chapter 8 are constructed in the Jacobian and Hessian in this chapter so that the system's performance can be computed up to the second-order while perturbations of the variables are present and confined within the sensitivities' range. The merit function's expansion, incorporating the first- and second-order sensitivities, enables the calculation of the updated merit function value. This chapter examines the accuracy of the expansion of the merit function in the analytical framework for the evaluation of dynamically perturbed optical systems. First, the Czerny-Turner spectrometer of chapter 8 is subjected to uniform thermal expansion. Subsequently, the computational time for vibrational analysis of the spectrometer is compared with the corresponding transient analysis in Zemax.

## 9.1. Thermal expansion

The Czerny-Turner spectrometer from chapter 8 includes optical elements floating in space. For this chapter, a simple mechanical housing is designed to hold all elements and is subjected to dynamic disturbances. The model is built in the Comsol environment, where the individual element displacements are found. In this section, the complete housing is heated by one degree from its nominal temperature, and the optical performance due to the displacements is evaluated. Before implementing this data into the analytical framework, the x displacement of the slit is subtracted from the x displacement of the optical elements. This data manipulation is performed since the x location of the ray is not considered in the formulation. The direction of the expansion is given in Figure 9.1, with its magnitude increased.

To allow the mechanical housing to expand homogeneously due to the heat load, the model is constrained with a pin and roller support as seen in Figure 9.1. The homogeneous expansion scales all dimensions with the same factor in relation to the thermal center. Due to the constraints, the thermal center is located in the lower left corner where the pin support is. For the thermal expansion, the change of the radii of the spherical mirrors is taken into account in the Taylor expansion. As a result of the uniform thermal expansion, the distance between the lines of the grating would increase and therefore become less dispersive. The sensitivity of the grating variable $d$ on the system's performance was not computed and therefore not taken into account for the homogeneous expansion. The spot size for the three wavelengths can be seen in Table 9.1 where the relative difference between the Taylor expansions is given to the analytical matrix formulation.

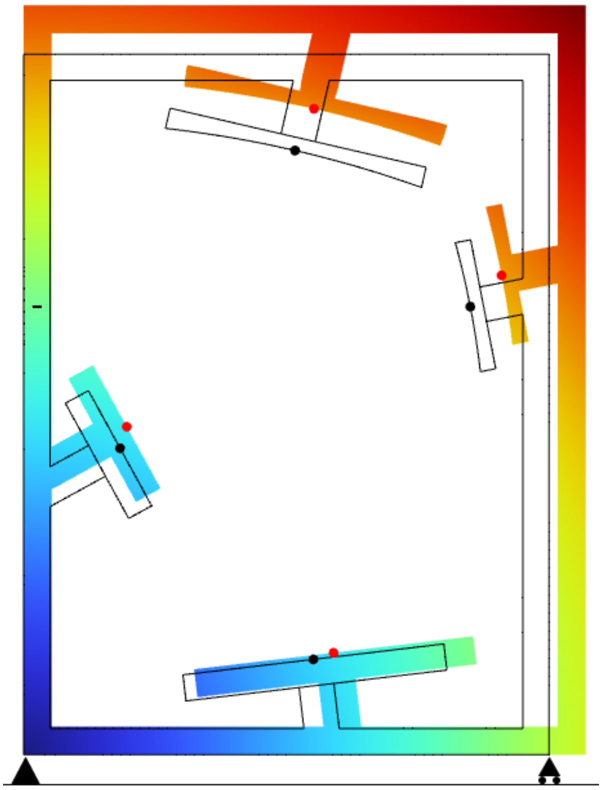

**Figure 9.1:** Mechanical housing of spectrometer with its support. The scale of the expansion due to the heating of one degree is exaggerated for review

**Table 9.1:** Results for spot size [mm] per wavelength [$\mu$m] after homogeneous expansion

| | $\lambda = 0.550$ | $\lambda = 0.700$ | $\lambda = 0.850$ |
|---|---|---|---|
| Analytical framework | 0.9418 | 0.7345 | 0.5506 |
| Taylor expansion ($J_f$) | 0.9418 | 0.7345 | 0.5506 |
| Relative difference | -4.049E-10 | -5.981E-10 | -9.243E-10 |
| Taylor expansion ($J_f + H_f$) | 0.9418 | 0.7345 | 0.5506 |
| Relative difference | -3.847E-10 | -8.034E-10 | -2.110E-09 |

In Table 9.1, the spot sizes computed by three different evaluation techniques are shown. The analytical framework multiplies all matrices and the Taylor expansion of the merit function is included with only the Jacobian ($J_f$) and the expansion with the Jacobian and Hessian ($J_f + H_f$). The relative difference between the two expansions to the analytical framework shows that the Jacobian by itself provides a strong approximation of the merit function, and the added accuracy of the Hessian is negligible, for this specific displacement field. To review the effect of the used displacement field, displacement by gravity is also introduced.

## 9.2. Displacement by gravity

This section introduces the displacements by gravity to the optical model and goes further into the effect on the accuracy of the Hession on the Taylor expansion. For this disturbance, the housing has a fixed constraint on the bottom and gravity is pulling on the housing in the positive x direction. The scale of the displaced housing, given by the colored frame in Figure 9.2, is exaggerated for review.

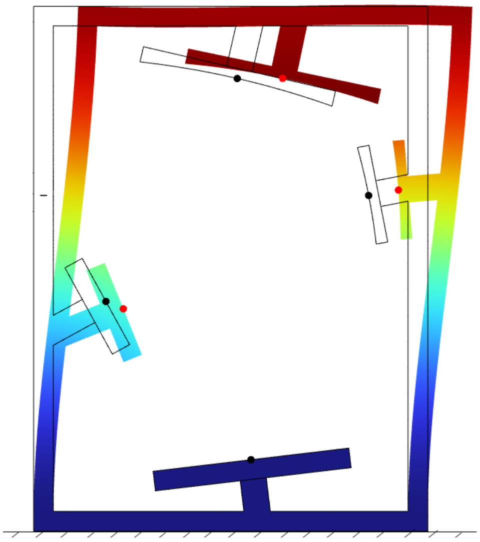

**Figure 9.2:** Deflection of the mechanical housing by gravity directed in the positive x direction. The scale of the deflection is exaggerated for review

The displacements of the slit are subtracted from the displacements of the optical elements in data pre-processing to account for disturbances in the slit. The rotation of the slit is also accounted for in data pre-processing, this rotation is subtracted from the rotation of the optical element, and the induced translation over the x and y-axis due to the rotation of an off-axis point is considered by

$$\begin{bmatrix} x' \\ y' \end{bmatrix} = \begin{bmatrix} cos(\theta_s) & -sin(\theta_s) \\ sin(\theta_s) & cos(\theta_s) \end{bmatrix} \begin{bmatrix} x \\ y \end{bmatrix}. \tag{9.1}$$

In this transformation, $\theta_s$ is the angle of the slit, and $x$, $y$ are the displaced but unrotated coordinates.

The spot size calculated by the two Taylor expansions and analytical framework is presented in Table 9.2. Again for this displacement field the improvement in the accuracy is negligible when the Hessian is added to the Taylor expansion. The displacement field for both the thermal expansion and gravity is relatively small to the overall dimensions of the optical system. To research the effect of larger displacements, the displacement field created by gravity is factorized. The results for this can be seen in Figure 9.3, where the absolute error of the two different Taylor expansions is plotted against the larger displacement fields.

**Table 9.2:** Results for spot size [mm] per wavelength [$\mu$m] for deflection due to gravity

| | $\lambda = 0.550$ | $\lambda = 0.700$ | $\lambda = 0.850$ |
|---|---|---|---|
| Analytical framework | 0.9418 | 0.7345 | 0.5506 |
| Taylor expansion ($J_f$) | 0.9418 | 0.7345 | 0.5506 |
| Relative difference | -2.076E-07 | -1.853E-07 | -9.777E-08 |
| Taylor expansion ($J_f + H_f$) | 0.9418 | 0.7345 | 0.5506 |
| Relative difference | -1.304E-07 | -1.360E-07 | -1.730E-08 |

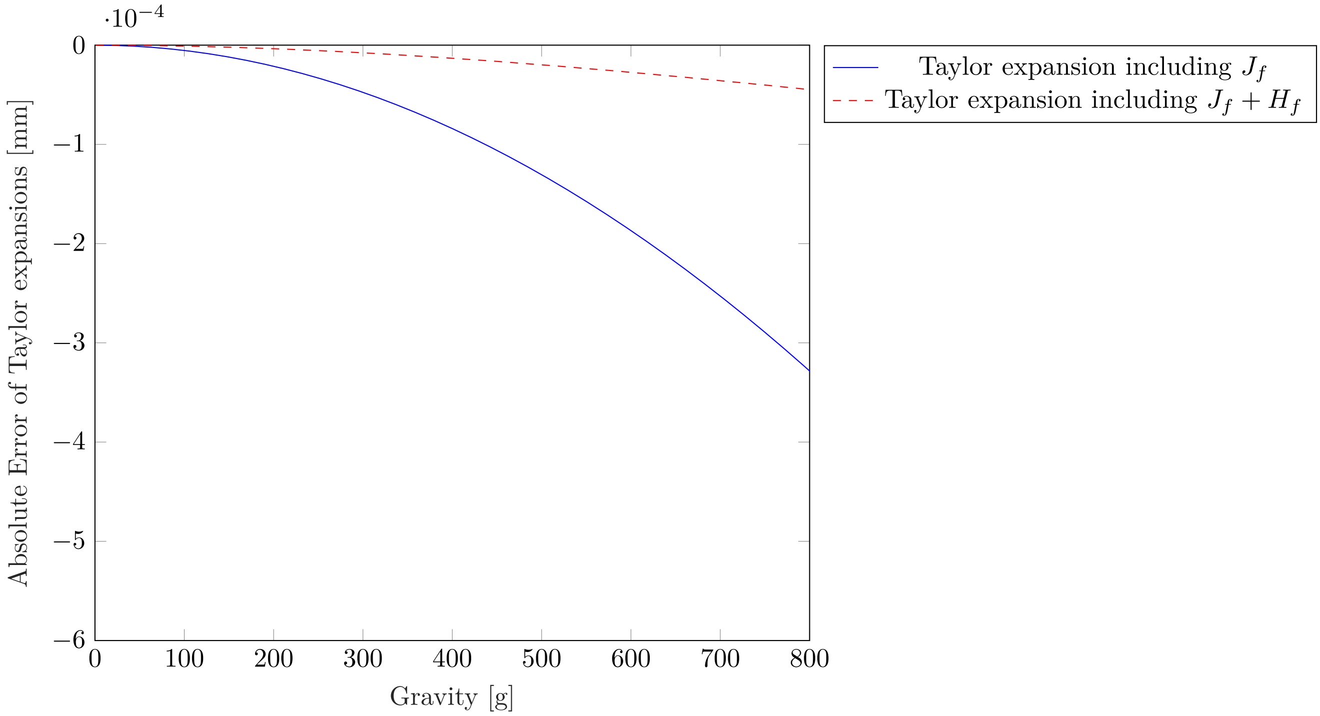

**Figure 9.3:** Absolute difference between both Taylor expansions and the analytical framework for $\lambda = 0.850$ $\mu$m

The difference between the absolute errors of both Taylor expansions in Figure 9.3 show that the Hessian significantly contributes to the approximation of the merit function at a gravity loading of 300g and larger. The maximum translation displacement of the optical elements at 300g is 0.6 mm and for rotation 0.0092 rad. This concludes that the effect of small perturbations can be accurately described by only the Jacobian for the specific merit function.

## 9.3. Vibration analysis

This section discusses the results found for the vibration analysis of the Czerny-Turner spectrometer. First, the boundary conditions of the model are explained and later the results found for the transient analysis in the analytical framework and Zemax are compared on accuracy and computation time.

For the vibrational analysis of the Czerny-Turner spectrometer, the boundary conditions are different in comparison to the thermal model but similar to the gravity loading. In the vibrational analysis, the mechanical housing has a fixed constraint on the bottom of the design and is subjected to a force in the positive x direction deployed in the upper left corner, this is depicted in Figure 9.4. As a result, the top part of the housing waves from left to right which is shown in Figure 9.5.

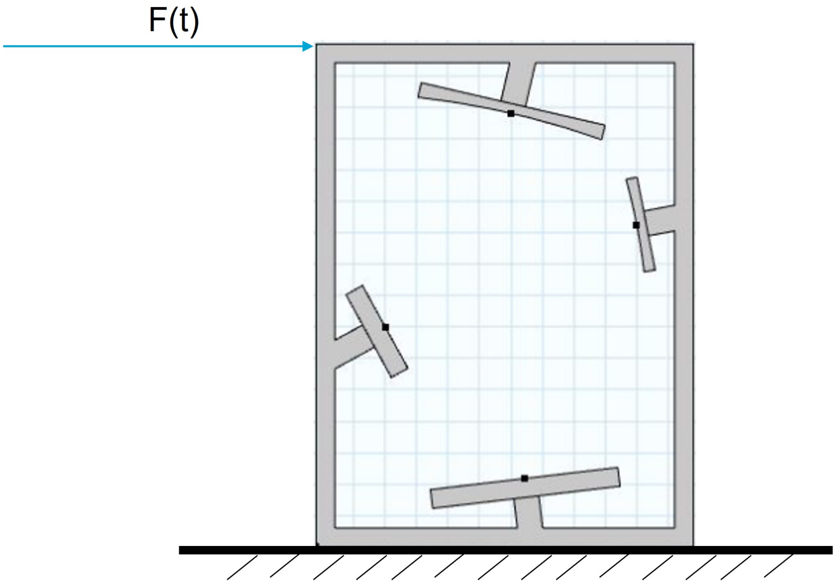

**Figure 9.4:** Schematic representation of applied load case for transient analysis of Czerny-Turner spectrometer. The mechanical housing is fixed on the bottom and a sawtooth wave is used for applied force with a frequency of 50 Hz.

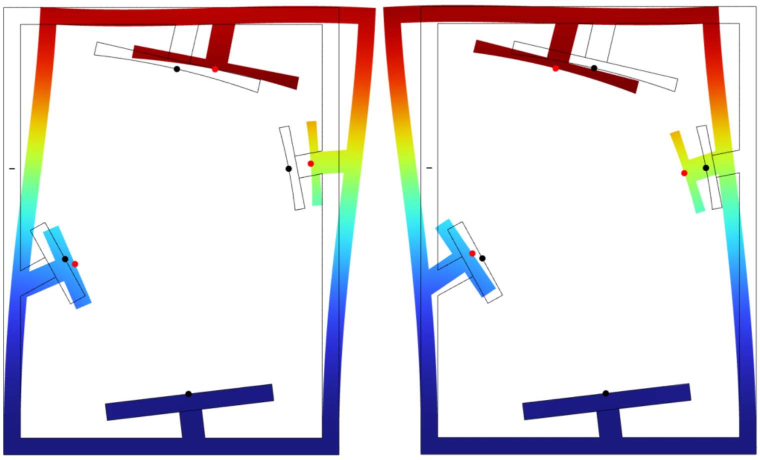

**Figure 9.5:** The result of vibration at t = 0.000765 (left), t = 0.007385 (right). The scale of the displacement field is exaggerated for review

The applied force differs over time by a sawtooth wave, or ramp waveform, with a frequency of 50 Hz. The displacements over time of the slit, two mirrors, grating, and detector are retrieved for 0.01 seconds with 2000 intermediate time steps. The displacement and induced rotation around the z-axis from the nominal position due to vibrations is plotted for each element in Figure 9.6 - Figure 9.8. Again, the data for the displacement field is pre-processed by subtracting the angle of the slit for the angle of the optical elements and constructing the new coordinates by Equation 9.1. Figure 9.6 - Figure 9.8 shows the pre-processed data where Figure 9.5 shows the physical displacement with a large scale for review.

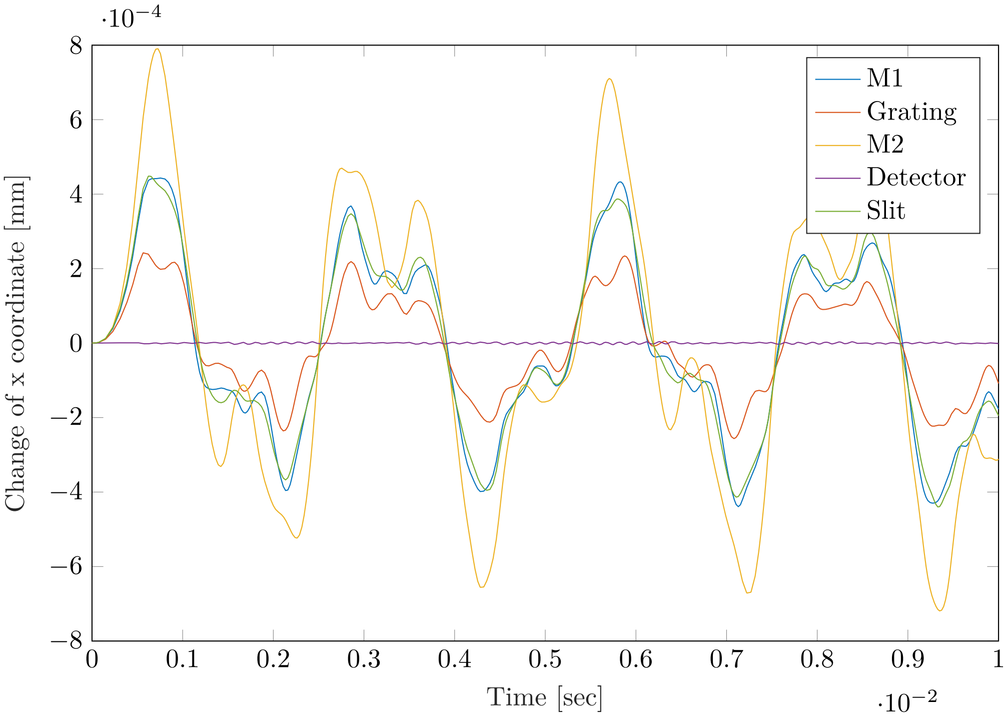

**Figure 9.6:** Change of x coordinate due to excitation of mechanical housing for all optical components over time

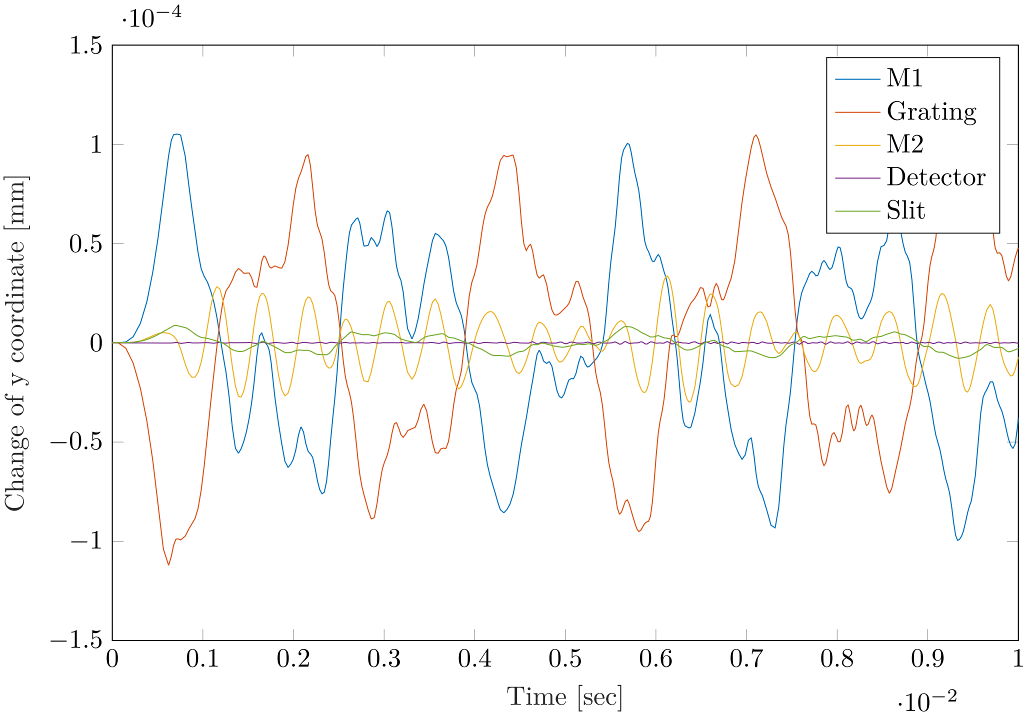

**Figure 9.7:** Change of y coordinate due to excitation of mechanical housing for all optical components over time

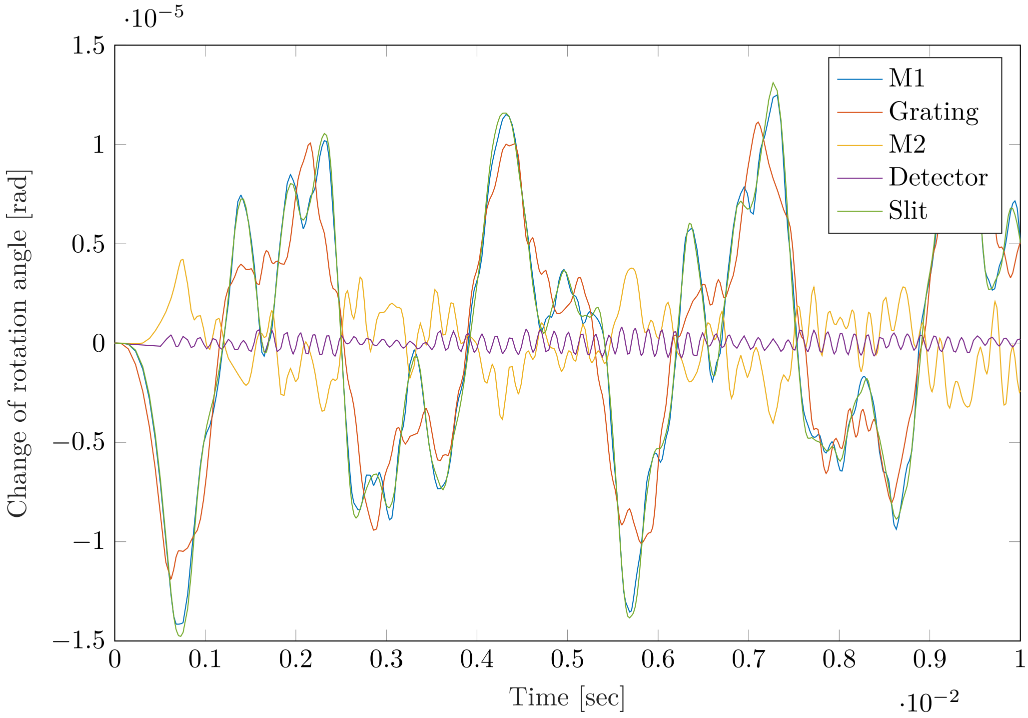

**Figure 9.8:** Change of rotation angle due to excitation of mechanical housing for all optical components over time

To retrieve the fastest computation time for the transient analysis in Zemax, the ZOS-API interface is again used. The obtained rigid body displacements are filled in for every time step in Zemax, and the spot size calculation is done. The interface uses Zemax as the ray trace engine and no computation time is wasted on the GUI from Zemax. The results on the spot size over time for the different wavelengths can be seen in Figure 9.9.

The different wavelengths show horizontal segments over time, the cause of this is the minimal decimal retrieval of the ZOS-API interface. Therefore for multiple consecutive timesteps, the value for the spot size is rounded to the same decimal number.

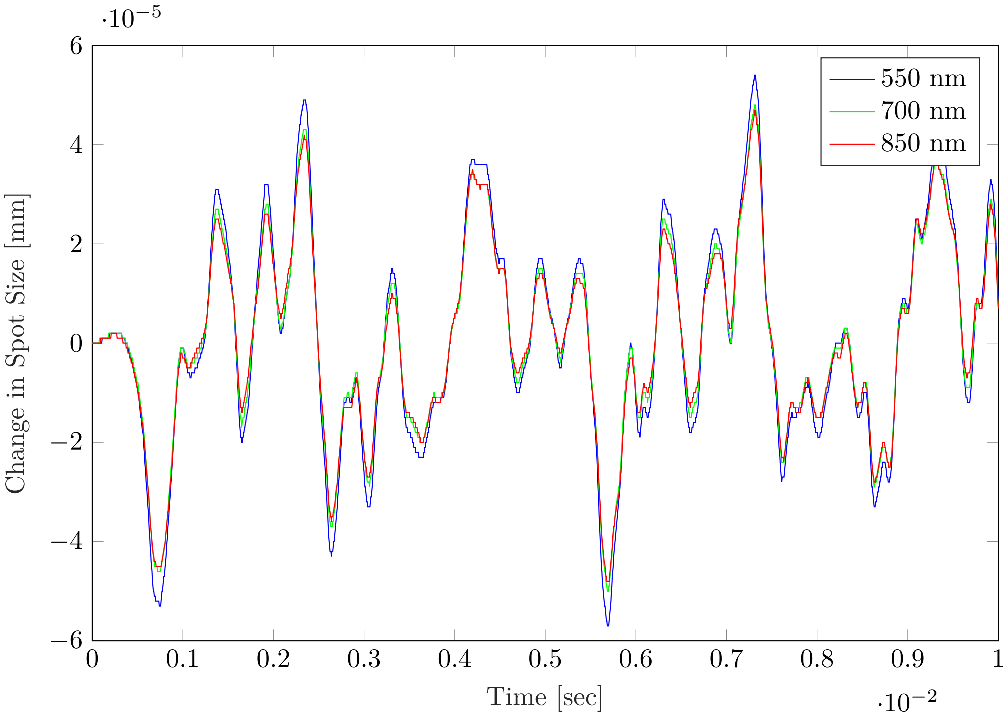

**Figure 9.9:** Transient analysis in Zemax on spot size for 3 wavelengths in perturbed spectrometer

In Figure 9.9 it can be seen that all wavelengths follow the same trend but have different magnitudes in the peaks and valleys. The same trend is as expected since all wavelengths propagate through the same optical system. The most striking result for this figure is that, for each minimum and maximum, $\lambda = 550$ has the most extreme magnitude. Since only one vibration mode is investigated for this research, it can not be concluded if the magnitude difference is due to the specific vibration mode or defaults in the model.

The transient analysis is also performed in the analytical framework, the results for this are seen in Figure 9.10 - Figure 9.12 for all wavelengths separately. The plots hold the data from the Zemax analysis in black and the data from the expanded merit function consisting of the Jacobian and Hessian in their respective color. Moreover, the change in performance is also shown for the analytical framework with the full matrix multiplication for each time step, these results are presented by the black dashed line. On the y-axis, the change in the nominal spot size of its respective method is plotted. Across all wavelengths, it can be seen that the analytical framework aligns with the trend observed in the Zemax analysis. However, the magnitude for the peaks has different accuracy across the observed spectrum.

In Figure 9.10, the magnitude of the analytical Taylor expansion underestimates for most of its peak, nevertheless, the steep increase or decrease in spot size mostly follows the analysis in Zemax. The analytical calculation overlaps well with the analytical Taylor expansion which concludes that the expansion of the merit function does not introduce the observed difference with the analysis in Zemax.

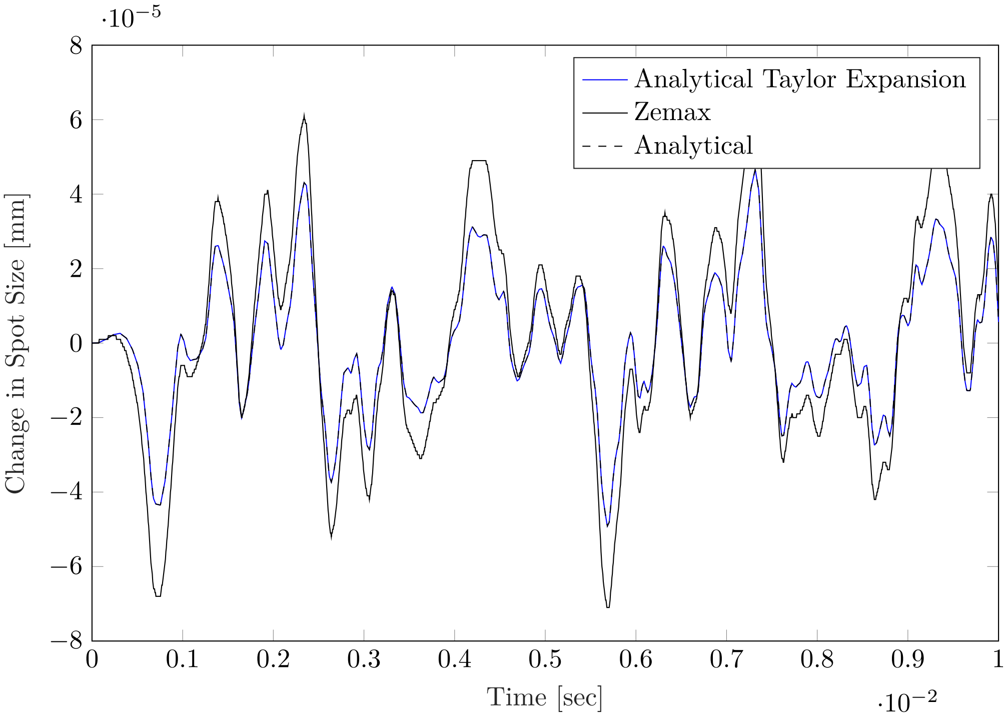

**Figure 9.10:** Change in spot size for $\lambda = 550nm$ computed by the analytical framework, its expansion and Zemax

For $\lambda = 700$ nm, the results obtained by the analytical Taylor expansion slightly underestimate the analysis in Zemax, but to a lesser degree than for $\lambda = 550$ nm. The good overlap is due to $\lambda = 700nm$, being close to the central wavelength of the grating. The central wavelength of a grating is found by

$$\Delta s = \lambda_c = d(sin(\alpha) + sin(\beta)), \tag{9.2}$$

and for the nominal design, $\lambda_c$ is found to be 696.3 nm [37]. In Equation 9.2, $\alpha$ is the incoming angle, $\beta$ the outgoing angle, $d$ the grating constant, and $\Delta s$ the extra path propagated for each inspected wavelength. The angles are determined by the nominal design, and the grating constant is also set. To find closer overlap for another wavelength, the grating constant can be changed. In conclusion, the effect of the linearization for only the incoming slope has less impact on the central wavelength.

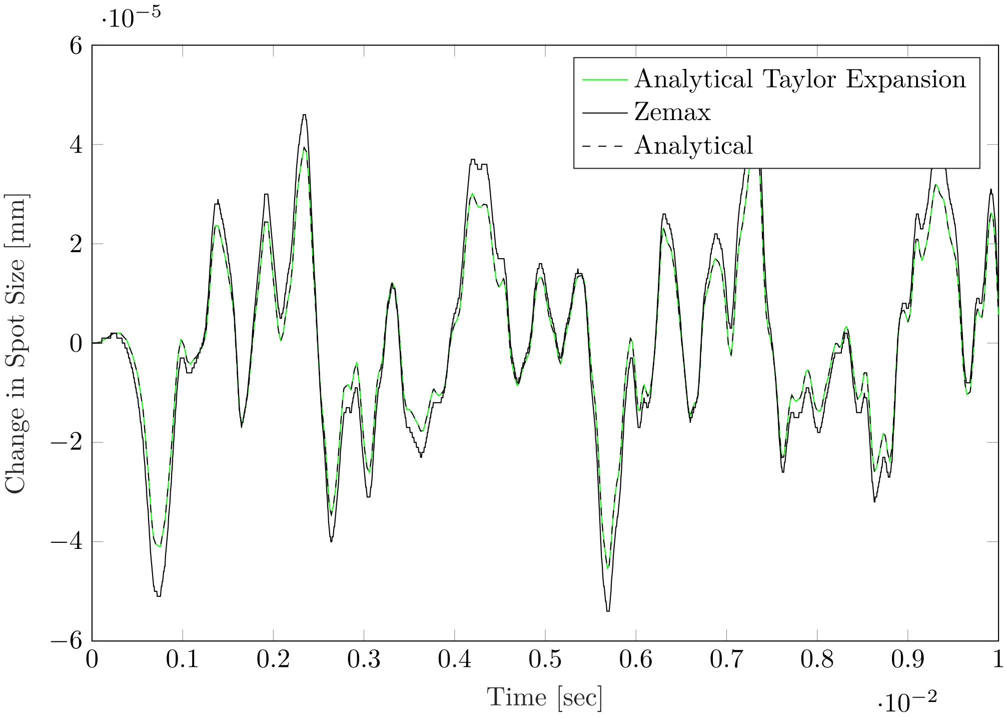

**Figure 9.11:** Change in spot size for $\lambda = 700nm$ computed by the analytical framework, its expansion and Zemax

In contrast to the change in the spot size for $\lambda = 0.550$ nm, the spot size difference for $\lambda = 850$ nm is overestimated by the analytical Taylor expansion. The Taylor expansion of the merit function does not introduce this difference, since the analytical analysis in the dashed black line overlaps with the expanded. The grating introduces a wavelength-dependent error, which is related to the difference seen in the plot. The quantification of this error is for further research, however, the first derivative of the grating function, as seen in Equation 7.3 becomes larger for larger wavelengths and therefore overestimates the added wavelength-dependent outgoing slope. This derivative is multiplied by the difference between the incoming slope of the marginal rays and the chief ray, which causes a larger difference for a diverging beam. The nominal design of the Czerny-Turner spectrometer holds a slightly diverging beam onto the grating, and therefore for wavelengths other than the central wavelength, an offset is created. The linearization leads to the consequence that the second mirror images the larger wavelengths with a greater spot size due to the linearization and vice versa for the smaller wavelengths.

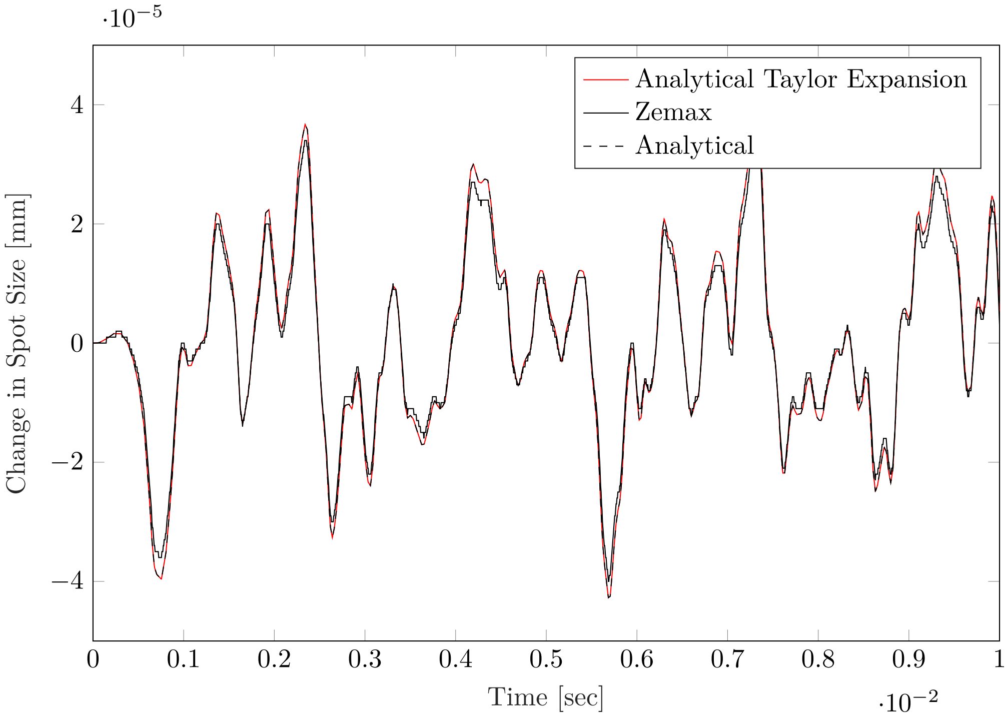

**Figure 9.12:** Change in spot size for $\lambda = 850nm$ computed by the analytical framework, its expansion and Zemax

For the comparison of the analytical Taylor expansion method for the evaluation of transient analysis of optical systems, its accuracy and computation time are compared to the equivalent paraxial analysis in Zemax and with the analytical framework. The accuracy is communicated by the Root Mean Square Error (RMSE) for the changes in the spot size. The RMSE values for the different wavelengths can be found in Table 9.3, as well as the time for completion of the transient analysis of all three wavelengths. The results are found by executing the analysis five times and taking the average.

**Table 9.3:** RMSE for change in spot size and computation time for analytical Taylor expansion method, Zemax analysis, and analytical method

| | Analytical Taylor expansion | Analytical method | Zemax |
|---|---|---|---|
| Computation time [s] | 0.02407 | 11.59 | 25.09 |
| RMSE [mm] for $\lambda = 550$nm | 6.60e-6 | 1.13e-5 | |
| RMSE [mm] for $\lambda = 700$nm | 1.10e-6 | 4.51e-5 | |
| RMSE [mm] for $\lambda = 850$nm | 4.27e-6 | 1.75e-6 | |

The conclusion on the computation time is that the newly proposed method for calculating the outcome of the transient analysis with an analytical Taylor expansion is faster by a factor of 1000. This comes at the cost of accuracy, which mainly is induced by the linearization of the grating. The maximum RMSE value for the analytical framework is 6.60e-6 [mm], which is small but not negligible due to the small magnitude of the overall change of the spot size.

## Change in location of spot

In chapter 5, the second merit function that is introduced in the analytical framework is the change in the location of the spot. The change in location for the three analyzed wavelengths can be seen in Figure 9.13. In this figure, the data on the location is collected via matrix multiplication in the analytical framework, instead of the Taylor expansion of the merit function.

The change in location is for all wavelengths similar in trend and magnitude. Important to note is the overall magnitude of the change since this indicates that the spot travels a larger distance over the detector than the change in spot size during the specific vibration. This causes the specific optomechanical design to be more faulty for the calibration of the detector in comparison to the ability to resolve the different wavelengths. Verifying the location change with Zemax is a suggestion for further research.

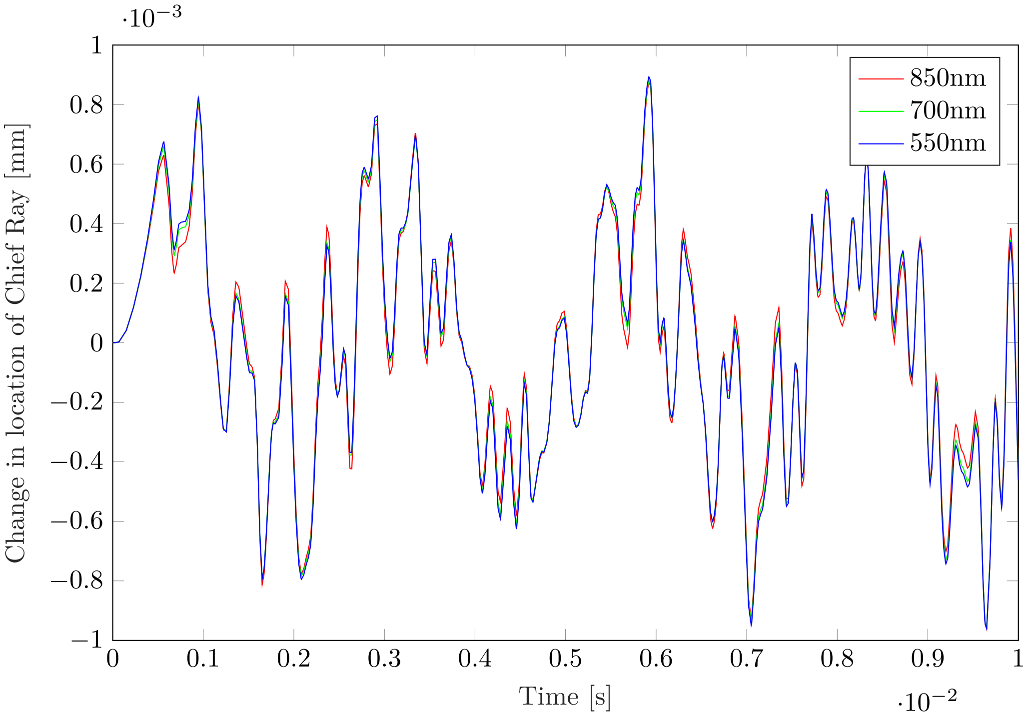

**Figure 9.13:** Change in location, for three wavelengths, of the chief ray on the detector of Czerny-Turner spectrometer

# 10

# Conclusion and recommendations

In this chapter, the conclusions on the results of the research are drawn. First, section 10.1 discusses the retrieved accuracies of the proposed method and the research contributions to the field. Second, the recommendations for further research in this field are elaborated in section 10.2.

## 10.1. Conclusion

This study demonstrates the effectiveness of sensitivity analysis in assessing the impact of dynamic disturbances on optical performance efficiently. The proposed analytical framework employs a Taylor expansion for the merit function and includes both the Jacobian and Hessian to decrease computation time in transient analysis.

During the establishment of the analytical framework, it became evident that the independent placement of optical elements in the system is crucial for researching rigid body displacements by the matrix method. The employed matrix formulation showed significant benefits over similar methods and allowed the merit function to be built modular, eliminating the necessity of information on previous elements, which also contributed to the easy retrieval of sensitivities.

The accuracy of the analytical framework was verified on the level of merit function computation without the Taylor expansion and the retrieved sensitivities. The error percentage on the magnitude of the first-order sensitivities of the two inspected optical models averaged within 0.22-0.5%, where the computation of the merit function for the spectrometer observed lower error percentages of 0.08-0.15% for an arbitrary case study.

Through a comparison with state-of-the-art optical analysis software, the proposed analytical framework showed an improvement in computation time for transient analysis of 1000x while the degradation in accuracy for the change in the spot size states a maximum RMSE value of 6.60e-6 mm for a nominal spot size of 0.94 mm. One of the objectives was to evaluate the enhancement of the approximation from the analytical framework by including second-order derivatives for the performance evaluation. It is determined that while researching spot size changes due to small perturbations, the Jacobian is sufficient for the approximation of the merit function via the Taylor expansion. Including the Hessian adds value to the approximation when researching larger displacement fields.

In conclusion, this thesis offers valuable insights into the effects of mechanical design on optical performance during dynamic disturbances, thus enabling improvements to avoid errors in optical measuring systems. Furthermore, the computational efficiency of transient analysis in multi-mirror optical systems can be significantly enhanced by leveraging the Taylor expansion of the merit function for small perturbations. The presented inexpensive method to determine sensitivities of optical performance analytically can be utilized in the Taylor expansion, time-dependent optomechanical analysis, or assist in developing new mechanical designs with the help of gradient-based optimization. Next to this, the propagation of uncertainty by the disturbed optical elements on the merit function during random vibrations may also be solved adequately with the found sensitivities.

## 10.2. Recommendations

Drawing from the conclusions outlined in the preceding section, this section offers recommendations for further research and possible extensions to the current analytical framework. The following suggestions are given:

The research into dynamic disturbances in chapter 9 is limited, since the current analytical framework does not allow the independent placement of the light source in the merit function. Consequently, the analytical framework does not enable obtaining the sensitivities of the rigid body placement of the slit. Pre-processing the data makes it possible to review the optical performance of certain dynamic disturbances, however, better insight into the coupled mechanical-optical performance can be generated when including the sensitivities for the placement and rotation of the source.

In chapter 3, the trade-off between multiple ray trace formulations is performed. Literature has shown that ray transfer matrix methods can include systems in 3D, aspherical elements, or both. The current framework allows ray tracing in one plane, however, the extension toward the analysis of systems in 3D is possible as stated by Dorst [10]. The applicability of the framework will increase when optical systems in 3D can be analyzed, but the definition of the current merit function would need to be reviewed. For the framework to analyze optical systems that hold aspherical elements the matrix formulation should be changed. As a solution, the formulation of Caron *et al.* [4] shows great potential, however the homogeneous expression of points and rays needs to be added to include independent placement of optical elements for the analysis of rigid body displacements.

In addition to transient analysis, the analytical sensitivities hold great opportunities for the design of coupled mechanical-optical interfaces in topology optimization. The classic topology optimizer minimizes rigid body displacements for all optical elements so that the optical performance remains constant during perturbations. The introduction of sensitivities on the optical performance enables coupled stiffness and enlarges the design space for the mechanical-optical interface of optical instruments. Future research on applying the analytical framework to designs created by topology optimization promises the creation of interfaces that are more resistant to dynamic perturbations.

During random vibrations, the response of the system's variables is commonly given in the frequency domain. The applicability of the analytical framework may be extended to the propagation of uncertainty on the merit function since the found sensitivities allow mechanical engineers to remain within the frequency domain to analyze the effects of random vibrations without the inclusion of optical software. From the frequency response on the system's variables, the standard deviation can be obtained, which in combination with the found sensitivities can calculate the standard deviation of the merit function by random vibrations.

# References

[1] Carl Blaurock et al. "Structural-thermal-optical performance (STOP) sensitivity analysis for the James Webb Space Telescope". In: *Optical Modeling and Performance Predictions II*. Vol. 5867. SPIE, Aug. 2005, p. 58670V. DOI: `10.1117/12.618697`.

[2] Florian Bociort. *Aberration balance in error functions calculated analytically.* Tech. rep. 1998.

[3] Biao Cao et al. "Modified ray transfer matrix method for accurate non-sequential ray tracing between arbitrary reflective mirrors". In: *Optics Express* 28.12 (June 2020), p. 17732. ISSN: 10944087. DOI: `10.1364/oe.393045`.

[4] Jérôme Caron and Stefan Bäumer. "Progress in freeform mirror design for space applications". In: SPIE-Intl Soc Optical Eng, June 2021, p. 64. DOI: `10.1117/12.2599322`.

[5] Jérôme Caron, Tiberiu Ceccotti, and Stefan Bäumer. "Progress in aberration theory for freeform off-Axis mirror systems". In: *Optics InfoBase Conference Papers*. Optica Publishing Group (formerly OSA), 2021. ISBN: 9781557528209. DOI: `10.1117/12.2603625`.

[6] Comsol. *Czerny-Turner Monochromator.* URL: `https://www.comsol.com/model/czerny-8211-turner-monochromator-19061`.

[7] Theodore A. Corcovilos. "Beyond the ABCDs: A projective geometry treatment of paraxial ray tracing using homogeneous coordinates". In: (May 2022). ISSN: 19432909. DOI: `10.1119/5.0083069`.

[8] Psang Dain Lin and Chia-Hung Lu. *Analysis and design of optical systems by use of sensitivity analysis of skew ray tracing.* Tech. rep. 2004.

[9] Psang Dain Lin and Chuang-Yu Tsai. *First-order gradients of skew rays of axis-symmetrical optical systems.* Tech. rep. 2007.

[10] Leo Dorst. *Paraxial Geometric Optics in 3D Through Point-Based Geometric Algebra.* Tech. rep.

[11] K. Dupraz et al. "The ABCD matrices for reflection and refraction for any incident angle and surface". In: *Optics Communications* 443 (July 2019), pp. 172–176. ISSN: 00304018. DOI: `10.1016/j.optcom.2019.03.041`.

[12] Robert E. Fisher, Biljana Tadic-Galeb, and Paul R. Yoder. *OPTICAL SYSTEM DESIGN.* Tech. rep. 2008. DOI: `10.1036/0071472487`.

[13] Grant R. Fowles. *Introduction to Modern Optics.* 2nd. Dover Publications, June 1989.

[14] Renee Gracey et al. "Structural, thermal, and optical performance (STOP) modeling and results for the James Webb Space Telescope integrated science instrument module". In: *Modeling, Systems Engineering, and Project Management for Astronomy VI.* Vol. 9911. SPIE, Aug. 2016, 99111A. ISBN: 9781510602014. DOI: `10.1117/12.2233641`.

[15] Luzia Hahn and Peter Eberhard. "Transient dynamical-thermal-optical system modeling and simulation". In: *Journal of the European Optical Society-Rapid Publications* 17.1 (Dec. 2021). ISSN: 19902573. DOI: `10.1186/s41476-021-00150-1`.

[16] Horiba Scientific. *Optical Signal to Noise Ratio and Stray Light.* 2023.

[17] Daniel Hull. *Metrology of Optical Systems PRECISION OPTICS SERIES.* Ed. by OP-TEC. 2015. ISBN: 9780985800642. URL: `http://www.op-tec.org`.

[18] Anastacia M. Hvisc and James H. Burge. "Alignment analysis of four-mirror spherical aberration correctors". In: *Advanced Optical and Mechanical Technologies in Telescopes and Instrumentation.* Vol. 7018. SPIE, July 2008, p. 701819. ISBN: 9780819472281. DOI: `10.1117/12.789881`.

[19] Michael J. Kidger. *Fundamental Optical Design.* SPIE, 2002, pp. 1–9. ISBN: 9780819439154.

[20] S. Koppen et al. “Topology optimization of multicomponent optomechanical systems for improved optical performance”. In: *Structural and Multidisciplinary Optimization* 58.3 (Sept. 2018), pp. 885–901. ISSN: 16151488. DOI: `10.1007/s00158-018-1932-4`.

[21] Psang Dain Lin. “Differential method for determining third-order derivative matrix of ray with respect to source ray variables at spherical boundary”. In: *Optics Express* 28.23 (Nov. 2020), p. 35306. ISSN: 10944087. DOI: `10.1364/oe.405571`.

[22] Psang Dain Lin and Chien-Sheng Liu. *Jacobian and Hessian matrices of optical path length for computing the wavefront shape, irradiance, and caustics in optical systems.* Tech. rep. 2012.

[23] Psang Dain Lin and Chia Hung Lu. “Modeling and sensitivity analysis of laser tracking systems by skew-ray tracing method”. In: *Journal of Manufacturing Science and Engineering* 127.3 (2005), pp. 654–662. ISSN: 10871357. DOI: `10.1115/1.1954790`.

[24] Psang Dain Lin and Chi Kuen Sung. “Matrix-based paraxial skew ray-tracing in 3D systems with non-coplanar optical axis”. In: *Optik* 117.7 (July 2006), pp. 329–340. ISSN: 00304026. DOI: `10.1016/j.ijleo.2005.10.004`.

[25] N Lindlein et al. *Focusing light with a deep parabolic mirror.* Tech. rep. 2159.

[26] Chenyang Lyu and Renjun Zhan. “STOP model development and analysis of an optical collimation system for a tactical high-energy laser weapon”. In: *Applied Optics* 60.13 (May 2021), p. 3596. ISSN: 1559-128X. DOI: `10.1364/ao.419554`.

[27] J.C. Maxwell. *A Dynamical Theory of the Electromagnetic Field.* Tech. rep. 1864. URL: `http://rstl.royalsocietypublishing.org/`.

[28] Optics for hire. *Using RMS wavefront error to evaluate optical quality.* June 2023.

[29] Mattis Osterheider et al. “A do-it-yourself Czerny-Turner spectrometer: atomic emission, absorption, reflection and fluorescence spectroscopy in natural sciences”. In: *Physics Education* 57.6 (Nov. 2022). ISSN: 13616552. DOI: `10.1088/1361-6552/ac8a85`.

[30] Mark C. Sanson and Keith Hanford. “Use of advanced sensitivity approach to novel optical compensation methods”. In: SPIE-Intl Soc Optical Eng, June 2018, p. 8. ISBN: 9781510619173. DOI: `10.1117/12.2311325`.

[31] Shanghai OPTICS. *Freeform Optics.* 2023.

[32] Paul Urbach. “RayOptics_replacing_Sections10.1&10.2”. Delft, 2023.

[33] Wikipedia. *Euclid’s Optics.* URL: `https://en.wikipedia.org/wiki/Euclid%27s_Optics`.

[34] Wikipedia. *Propagation of uncertainty.* URL: `https://en.wikipedia.org/wiki/Propagation_of_uncertainty`.

[35] Wei Wu et al. “Research on Applicability of Sensitivity Table Method in Optical System Alignment”. In: *IOP Conference Series: Earth and Environmental Science.* Vol. 440. 3. Institute of Physics Publishing, Mar. 2020. DOI: `10.1088/1755-1315/440/3/032027`.

[36] Jie Yuan, Xingwu Long, and Meixiong Chen. *Generalized ray matrix for spherical mirror reflection and its application in square ring resonators and monolithic triaxial ring resonators.* Tech. rep. 1. 2011, pp. 1909–1917.

[37] Zemax. *How to build a spectrometer - theory.* Feb. 2024.

[38] Zemax. *https://support.zemax.com/hc/en-us/articles/1500005487921-ZOS-API-NET-An-Overview.* Mar. 2024.

[39] Thomas Zeschke et al. “Surface deformations of optical elements - An investigation of optical systems using the BESSY-NOM”. In: *AIP Conference Proceedings.* Vol. 879. 2007, pp. 679–682. ISBN: 0735403732. DOI: `10.1063/1.2436153`.

# A

# Comparison optical performance methods

From the trade-off made in chapter 3 it was concluded to further research both the matrix method from Dain Lin *et al.* [9] and Corcovilos [7]. In this chapter, both methods are implemented for the optical performance calculation of a simple model to investigate possible implications. First, the model is presented and its variables. Second, the results of both methods are compared with Snell's law on reflection and lastly, the obtained differences are discussed.

## The model

The initial implementation of both ray tracing matrix methods utilizes a basic model featuring a flat mirror folded at a 45-degree angle. To highlight the differences between the two methods, light rays within the system are only propagating in 2D rather than 3D. The model is illustrated schematically in Figure A.1, indicating that the optical axis aligns with the x-axis towards the mirror. Following reflection, the optical axis becomes parallel to the y-axis and travels in the negative direction. The placement of the light beam on the $y = -5$ line is being investigated with this model. Moreover, the accuracy of this crossing and the necessary work for extraction is of interest.

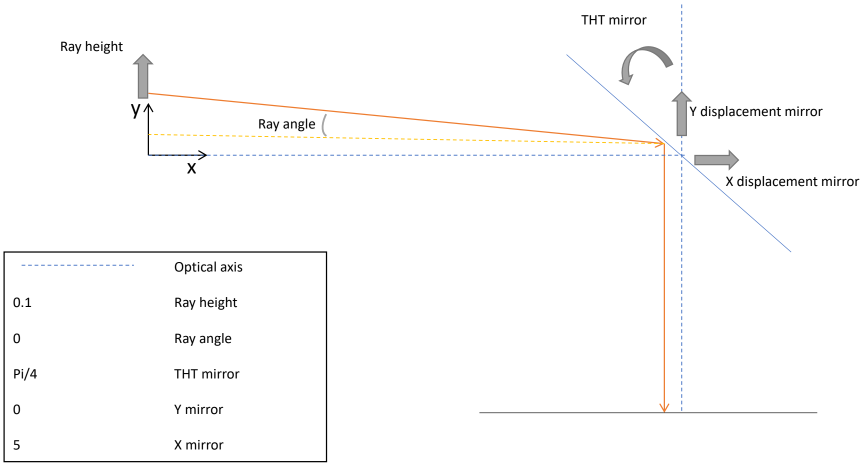

**Figure A.1:** Second subfigure

The model examines the rigid body movements of the mirror and the two variables associated with the ray, which are the height from the origin and the angle relative to the optical axis. As a result, the total number of variables in the system is five, which will be assessed for a single-variable parametric study. For each study, the remaining variables are maintained at their nominal values, which values are detailed in Table A.1.

**Table A.1:** Variables in the simple model and its value in nominal state

| Variable | Value | |
|---|---|---|
| $\theta_m$ | pi/4 | [rad] |
| $x_m$ | 5 | [mm] |
| $y_m$ | 0 | [mm] |
| $r_h$ | 0.1 | [mm] |
| $r_a$ | 0 | [rad] |

For this analysis, the rigid body motions of the image plane are neglected. Next to this, the variables present in the method of Dain Lin for the description of rays in 3D are disregarded since no comparison for these is possible by the method of Corcovilos.

## Results

This section will elaborate on the results of both methods, on the cross-section of the ray with the detector, in comparison to Snell's law. This study is performed by a parametric study on each variable of the folding mirror to examine the impact on the location of the intersection. Overall, it was found that the method of Dain Lin required adjustments to suit the use case of acquiring sensitivities. For that reason, an additional line is included in each plot to show the results of the adjusted method.

The verification method for the comparison is Snell's law, which states that the angle of incidence on the mirror is the angle of reflection from the mirror as given by Equation 2.1. This baseline is plotted in both Figure A.2 and Figure A.3 with a red dashed line. For the matrix methods to demonstrate satisfactory performance, the parametric study should closely adhere to the baseline.

Figure A.2 shows the shifting of the mirror in the x direction. As expected, Snell's law indicates a linear relation since the ray angle in the nominal system is equal to 0. The blue line indicates the parametric study done by the Corcovilos method and shows great resemblance to Snell's law for x displacement of the folded mirror. Contrary to this is the offset seen for the results obtained by the method of Dain Lin. The pink dashed line indicates that the intersection of the ray with the $y = -5$ line does not change, which is false. The same is observed for the y displacement of the mirror, which is fundamentally identical to the results seen for x displacement since the angle of the mirror is 45 degrees.

Both Figure A.2 and Figure A.3d also have a pink dash-dot line in which the coordinate system of the image plane is shifted with the added displacement on the mirror. The parametric study shows that the optical performance calculation is wrong, however, the slope of the line is parallel to Snell's law which indicates valuable sensitivities for these variables. Next to this, the method of Corcovilos shows a similarity to Snell's law for the displacement in y.

The parametric study of the rotation of the mirror can be seen in Figure A.3c. Again for this variable Corcovilos follows Snell's law. The pink dashed line of Dain Lin shows a non-linear relation as expected for the rotation of the folded mirror. However, it deviates from Snell's law. The cause of this is unknown but most likely related to the desired coordinate changes as discussed for the x and y displacement.

For both variables regarding the incoming ray, the parametric study can be seen in Figure A.3a and Figure A.3b. The study on the ray angle holds an offset with regard to Snell's law for Dain Lin. Moreover, the slope of Dain Lin differs slightly from the baseline but remains in an acceptable range. For the ray height, the slope of Dain Lin is out of the acceptable range. Next to this, the parametric study of Corcovilos shows satisfactory results for both the ray angle and the ray height.

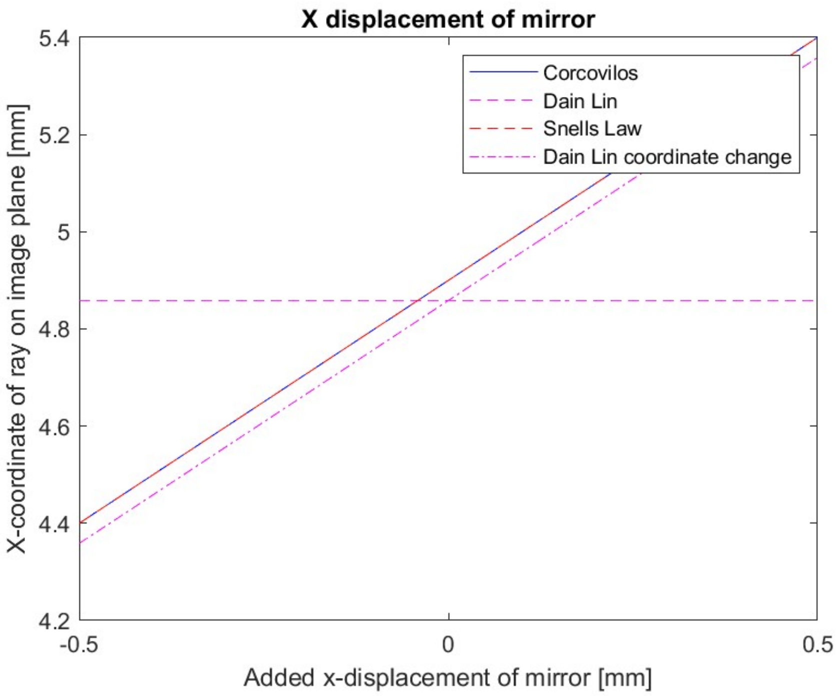

**Figure A.2:** X displacement of mirror

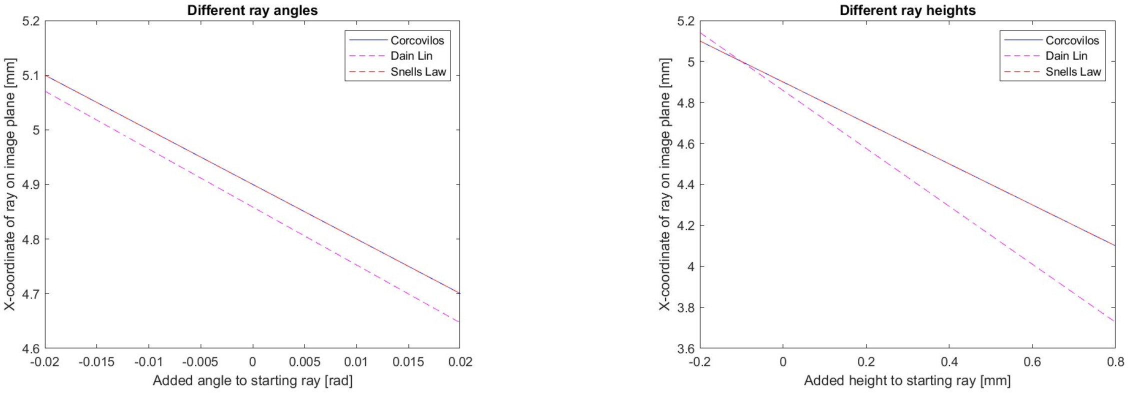

**(a)** Varying ray angles **(b)** Varying ray height

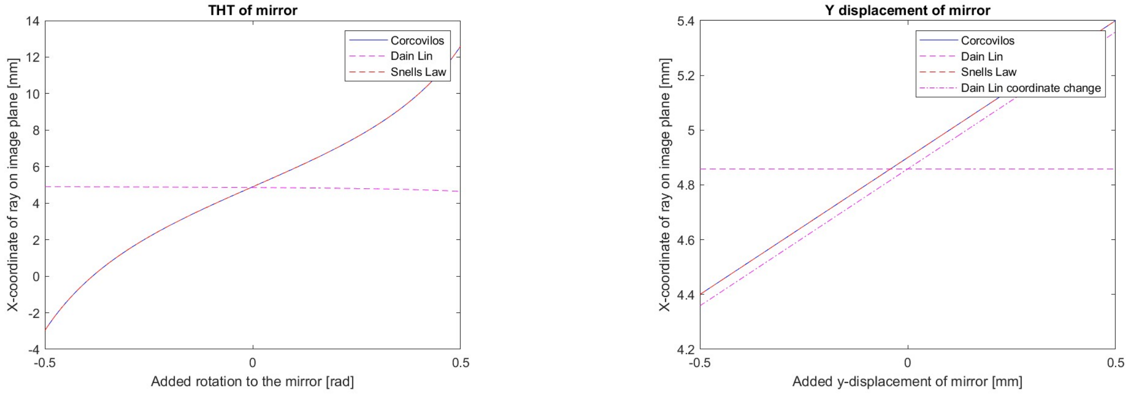

**(c)** Varying angle of mirror **(d)** Varying Y displacement of mirror

**Figure A.3:** Varying parameters in model for verification on the performance of both ray tracing methods with respect to Snell's law

## Coordinate system Dain Lin

The required coordinate change of the image plane for both the x and y displacement shows a dependency of the coordinates to the intersection of the ray. As seen in Figure A.2, the shifting of the mirror's coordinate system in the x direction does not affect the crossing of the ray on the detector plane when calculated by the method of Dain Lin. When the same x displacement is added to the coordinate system of the detector plane, the crossing with the detector plane follows Snell's law with a slight offset.

The method of Dain Lin superimposes and propagates errors from the origin of one coordinate system onto the next coordinate system. The orientation of these coordinate systems in the model can be seen in Figure A.4. The y-axis aligns with the optical path and undergoes rotation at mirror surfaces, ensuring perpendicular alignment to the surface and pointing away from the reflection. Due to the dependency of the placement, and thus rigid body displacements, of optical elements finding cross-dependent sensitivities for an optical system becomes complicated. Next to this, adding to the method to counteract this phenomenon might be a solution however, this is one of the criteria as discussed in the beginning of Appendix A. [1]

---

[1] During the implementation of the formulation for the simple model, contact with the writer was achieved. The conversation was via exchanging brief emails. It was found that the rays were not crossing/touching the image plane, hence this matter was communicated to the writer. Since the scientific topics of the writer had shifted over the years, the program used for the article was not up to date and there was no time to go into depth on this question. Next to this, the sensitivities obtained in an article from 2005[23] were found using finite differencing instead of an analytical approach. Hence, utilizing the method for analytical sensitivities was discouraged.

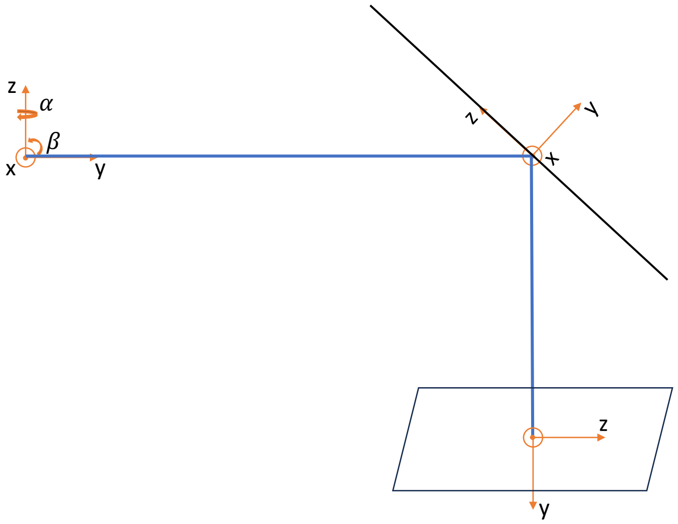

**Figure A.4:** Coordinate system orientation for Dain Lin method

## Conclusion

The parametric studies performed on the folded mirror conclude that the method of Corcovilos follows Snell's law closely, contrary to the method of Dain Lin, and will be used throughout this research as the analytical optical performance calculation method. Both methods are tested on accuracy and the necessary work for implementation in this chapter. It was found that the dependency of rigid body displacements in the method of Dain Lin could be overcome but would imply adding to the existing theory before application. This is set to be out of the scope of the research and therefore the matrix formulation of Corcovilos performs better in both criteria. In chapter 4, the novelty of this method is explained in further detail.

# B

# Model verification plots

## Difference plots for parametric study

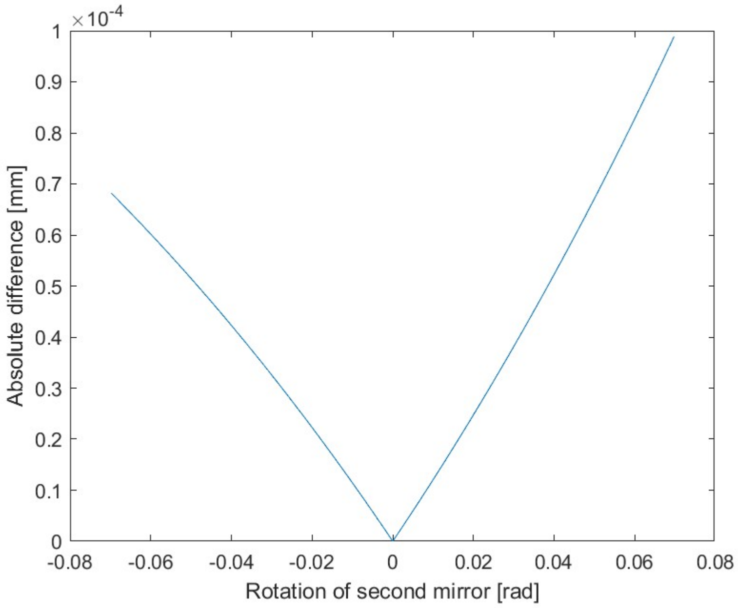

**Figure B.1:** Absolute difference of parametric study in Zemax and analytical framework, for rotation of second mirror

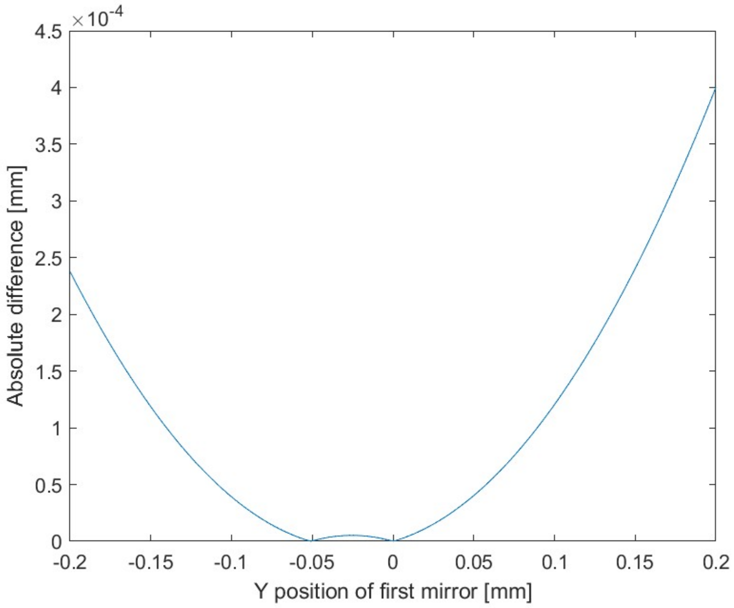

**Figure B.2:** Absolute difference of parametric study in Zemax and analytical framework, for Y position of first mirror

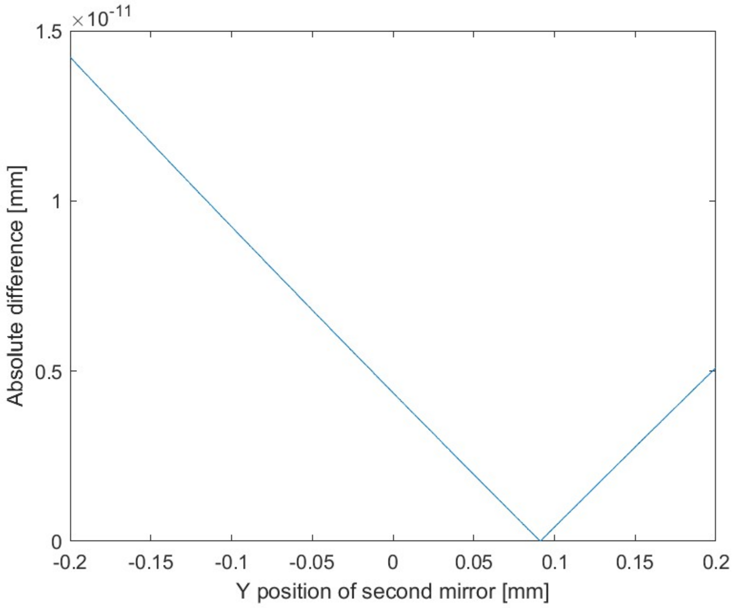

**Figure B.3:** Absolute difference of parametric study in Zemax and analytical framework, for Y position of second mirror

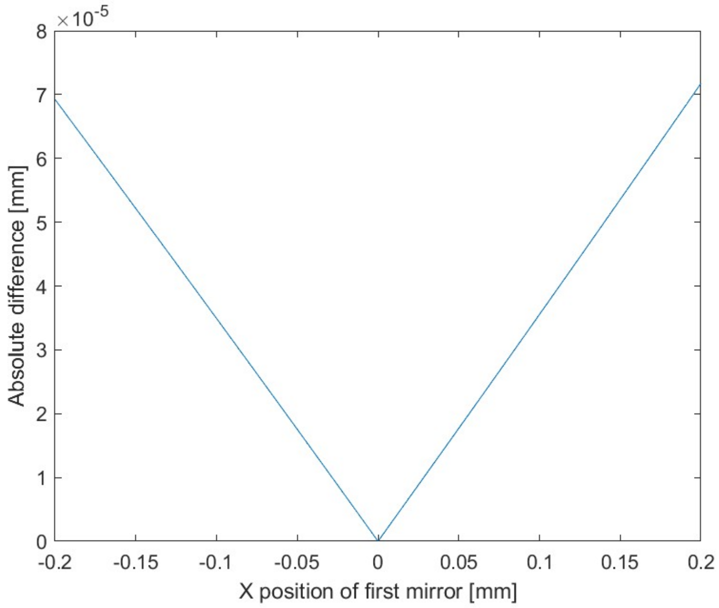

**Figure B.4:** Absolute difference of parametric study in Zemax and analytical framework, for X position of first mirror

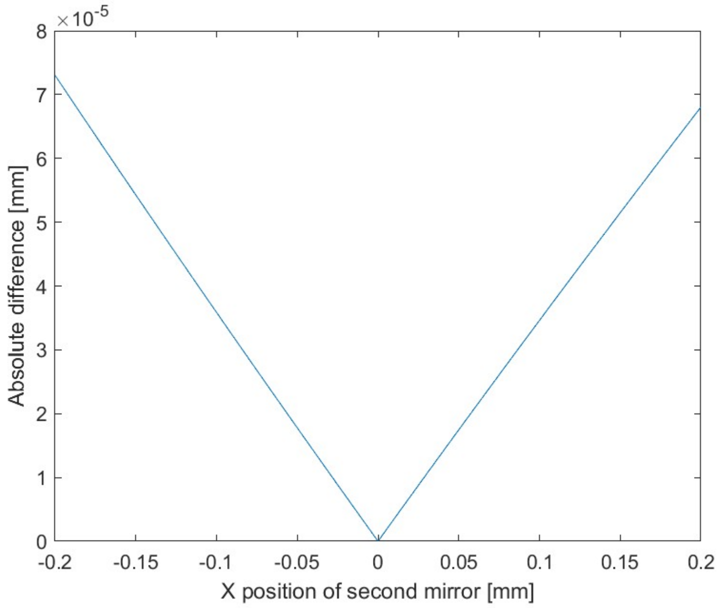

**Figure B.5:** Absolute difference of parametric study in Zemax and analytical framework, for X position of second mirror

# Step size plots

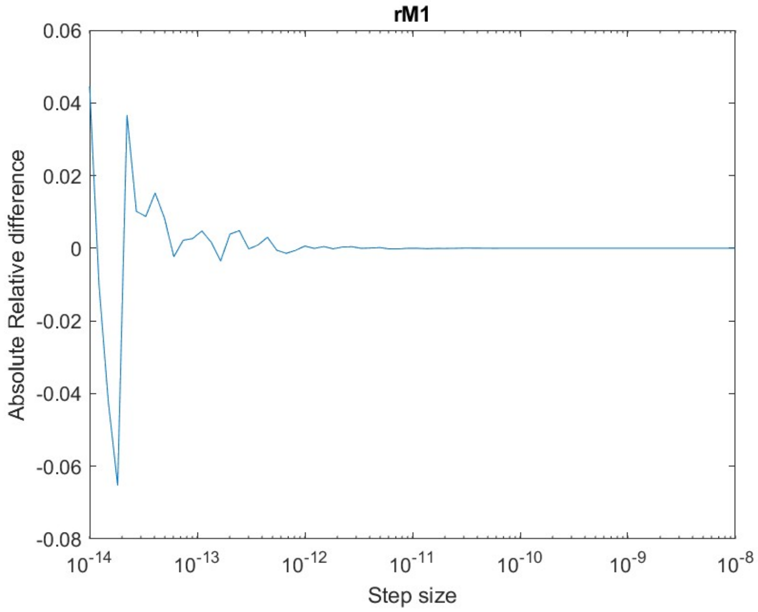

**Figure B.6:** Absolute relative difference between analytical and finite differencing of analytical framework, for variable rM1

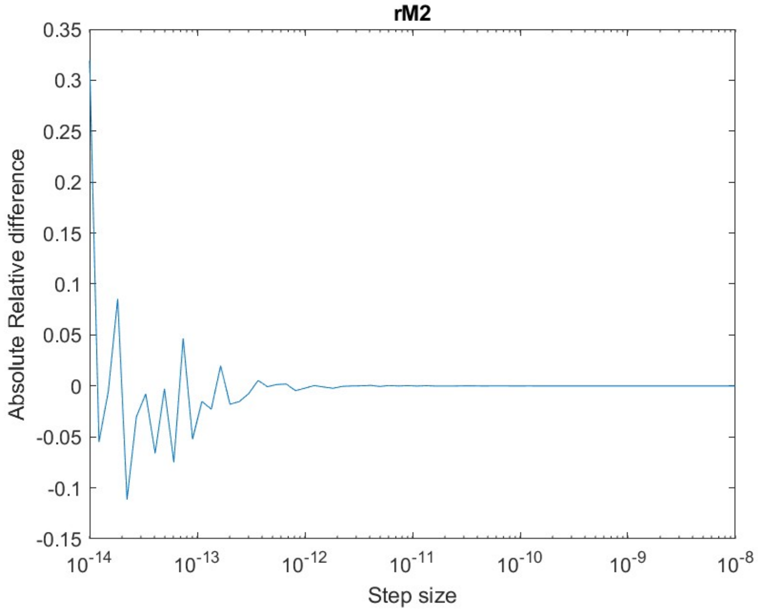

**Figure B.7:** Absolute relative difference between analytical and finite differencing of analytical framework, for variable rM2

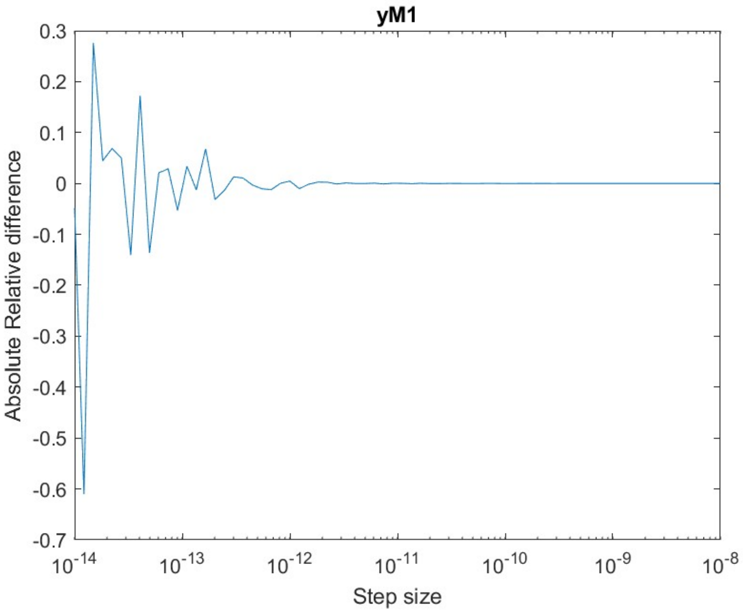

**Figure B.8:** Absolute relative difference between analytical and finite differencing of analytical framework, for variable yM1

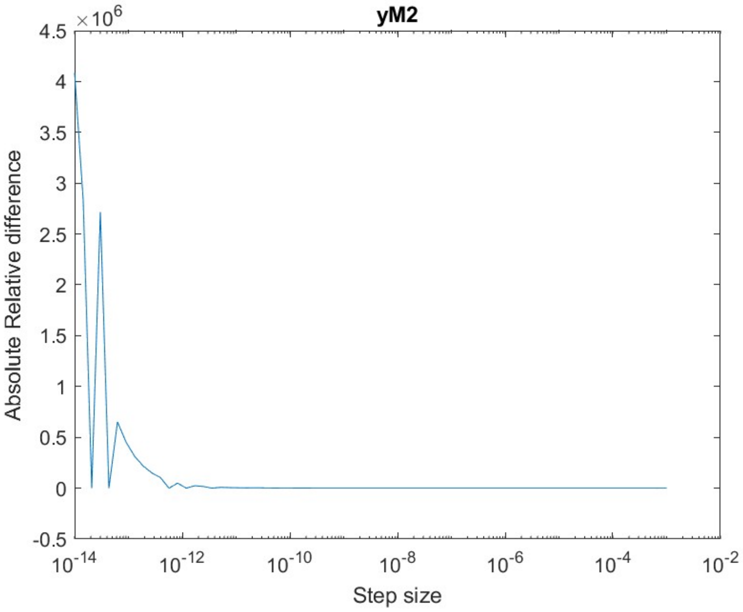

**Figure B.9:** Absolute relative difference between analytical and finite differencing of analytical framework, for variable yM2

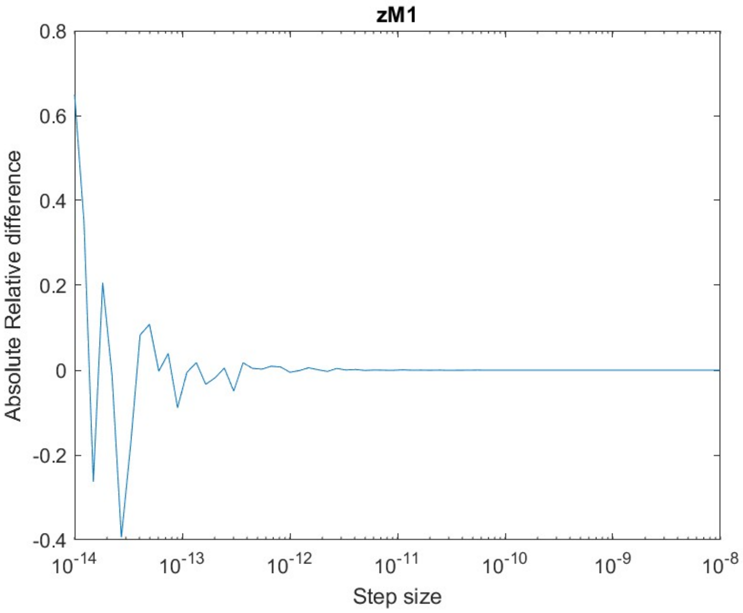

**Figure B.10:** Absolute relative difference between analytical and finite differencing of analytical framework, for variable zM1

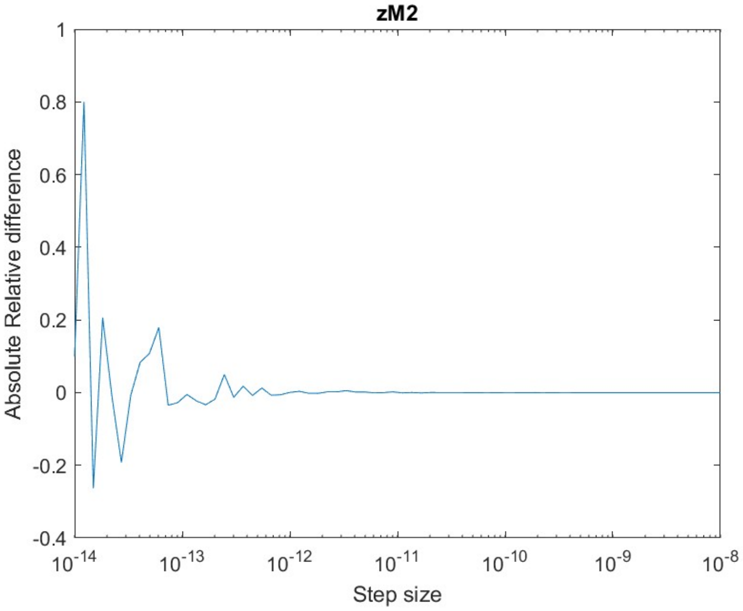

**Figure B.11:** Absolute relative difference between analytical and finite differencing of analytical framework, for variable zM2